



Variable Stars in M31 Stellar Clusters from the Panchromatic Hubble Andromeda Treasury

Richard Smith¹ , Avi Patel² , Monika D. Soraisam¹ , Puragra Guhathakurta³ , Pranav Tadepalli⁴ , Sally Zhu⁵ , Joseph Liu⁶ , Léo Girardi⁷ , L. Clifton Johnson⁸ , Sagnick Mukherjee³ , Knut A. G. Olsen⁹ , and Benjamin F. Williams¹⁰

¹ NSF's National Optical-Infrared Astronomy Research Laboratory, Gemini North, 670 North Aohoku Place, Hilo, HI 96720, USA; richard.smith@noirlab.edu

² Division of Engineering and Applied Science, California Institute of Technology, Pasadena, CA 91125, USA

³ Department of Astronomy and Astrophysics, University of California Santa Cruz, 1156 High Street, Santa Cruz, CA 95064, USA

⁴ Georgia Institute of Technology, Atlanta, GA 30332, USA

⁵ Stanford University, Stanford, CA 94305, USA

⁶ University of Southern California, Los Angeles, CA 90007, USA

⁷ Osservatorio Astronomico di Padova—INAF, Padova 35136, Italy

⁸ Center for Interdisciplinary Exploration and Research in Astrophysics (CIERA) and Department of Physics and Astronomy, Northwestern University, 1800 Sherman Avenue, Evanston, IL 60201, USA

⁹ NSF's National Optical-Infrared Astronomy Research Laboratory, 950 North Cherry Avenue, Tucson, AZ 85719, USA

¹⁰ Astronomy Department, University of Washington, Seattle, WA 98195, USA

Received 2024 April 10; revised 2024 July 30; accepted 2024 August 7; published 2024 October 17

Abstract

Variable stars in stellar clusters can offer key constraints on stellar evolution and pulsation models, utilizing estimates of host cluster properties to constrain stellar physical parameters. We present a catalog of 86 luminous ($F814W < 19$) variable stars in M31 clusters identified by mining the archival Panchromatic Hubble Andromeda Treasury (PHAT) survey using a combination of statistical analysis of sparse PHAT light curves and difference imaging. We determine the evolutionary phases and initial masses of these variable stars by matching them with theoretical isochrones generated using host cluster properties from the literature. We calculate the probability of PHAT photometry being blended due to the highly crowded nature of cluster environments for each cluster-variable star, using these probabilities to inform our level of confidence in the derived properties of each star. Our 86 cluster-variable stars have initial masses between 0.8 and $67 M_{\odot}$. Their evolutionary phases span the main sequence, more evolved hydrogen- and helium-burning phases, and the post-asymptotic giant branch. We identify numerous candidate variable star types: RV Tauri variables, red supergiants, and slowly pulsating B-type supergiants, along with Wolf-Rayet stars, α Cygni and Mira variables, a classical Cepheid, and a possible supersympotic giant. We characterize 12 cluster-variable stars at higher confidence based on their difference image quality and lower blending probability. Ours is the first systematic study of variable stars in extragalactic stellar clusters leveraging the superior resolution of the Hubble Space Telescope and demonstrating the unique power of stellar clusters in constraining the fundamental properties of variable stars.

Unified Astronomy Thesaurus concepts: Variable stars (1761); Andromeda Galaxy (39); Hubble Space Telescope (761); Star clusters (1567)

Materials only available in the [online version of record](#): machine-readable table

1. Introduction

Stellar clusters provide valuable insights into stellar evolution due to their constituent stars thought to have largely formed from the same material at the same time, resulting in stars with homogeneous metallicities and ages. This leaves stellar mass as the only significant variable between cluster members, allowing models of stellar evolution at measured cluster ages and metallicities to be tested.

By examining clusters of different ages, we can understand the evolution of star formation in a galaxy at different epochs (L. C. Johnson et al. 2017). However, interstellar dust dominates the galactic plane of the Milky Way, limiting the scope of stellar population studies in our galaxy (D. J. Marshall et al. 2006), complicated further by differing dust densities, and thereby extinction laws, depending on sight lines (G. Zasowski et al. 2009; C. González-Fernández et al. 2014; A. Saha et al.

2019; S. Wang & X. Chen 2019; R. Zhang et al. 2023). Extragalactic clusters have provided a solution to expanding the study of stellar populations in various environments, such as starburst galaxies (e.g., S. Lim et al. 2013 and references therein). However, it is a challenge to resolve these distant sources into stars, including using instruments such as the Hubble Space Telescope (HST). This in turn inhibits our ability to perform photometry on sources within clusters and thereby constrain various ensemble parameters such as cluster age and metallicity. M31 offers an ideal laboratory for studying stellar evolution, containing individual stars resolvable by HST thanks to its close proximity while also hosting stars of all ages (A. M. N. Ferguson et al. 2005; E. J. Bernard et al. 2012; B. F. Williams et al. 2017) and a large number of clusters (L. Clifton Johnson et al. 2015).

Variable stars in clusters are fundamental probes for studying both stellar pulsation and evolution (J. Zhuo et al. 2021; D. B. Palakkatharappil & O. L. Creevey 2023). A majority of the work on cluster-variable stars has focused on high-amplitude variables such as Cepheids, which have been used to calibrate the Cepheid period–luminosity relation



Original content from this work may be used under the terms of the [Creative Commons Attribution 4.0 licence](#). Any further distribution of this work must maintain attribution to the author(s) and the title of the work, journal citation and DOI.

through main-sequence (MS) fitting procedures (M. Feast 1999; C.-C. Ngeow & S. M. Kanbur 2004; D. Turner & J. Burke 2007). Period–age and period–age–color relations for Cepheids (G. Bono et al. 2005; R. I. Anderson et al. 2016; G. E. Medina et al. 2021) have also been calibrated via isochrone fitting of Cepheid-hosting clusters. Recently, asteroseismology in low-amplitude variables in stellar clusters has gained increased attention due to its ability to inform models of stellar interiors and stellar evolution (M. R. Templeton et al. 1997; S. Hekker et al. 2011). In particular, such studies allow measurements of stellar masses, radii and ages (e.g., red giant branch, RGB, stars in open clusters; S. Hekker et al. 2011; A. Miglio et al. 2012; M. H. Pinsonneault et al. 2018), providing further constraints for stellar models.

Extragalactic time-domain studies of variable stars have also been pivotal in our understanding of stellar physics. C. Conroy et al. (2018) studied variability in M51 using HST data to chart variability in the luminous regions of the color–magnitude diagram (CMD). M. D. Soraisam et al. (2020) examined the variability of massive stars in M31, finding an increasing prevalence of variability in later spectral types, with redder stars displaying larger fluctuations than bluer stars (see their Figure 8). A key hindrance with these studies is a lack of physical parameters (e.g., mass) for the stars. Constructing a statistical sample of variables in extragalactic stellar clusters will help us better understand stellar variability by leveraging the estimates of host cluster properties providing constraints on stellar physical parameters.

Historically, due to its large angular size, ground-based studies of variable stars in M31 are often limited in scope, focusing on field star populations in targeted OB associations or portions of the halo (P. Massey et al. 1986; J. Mould & J. Kristian 1986; C. J. Pritchett & S. van den Bergh 1988; A. W. McConnachie et al. 2009), though larger surveys and monitoring projects have also been conducted recently (e.g., C. H. Lee et al. 2012; M. D. Soraisam et al. 2020). The resulting photometry was typically limited to only the brightest field stars in such studies due to the low angular resolution available from ground-based observations. Additionally, due to their abundance and proximity, globular clusters in the M31 halo have been extensively cataloged and studied using ground-based telescopes (S. Galleti et al. 2004; M. B. Peacock et al. 2010; Y. Kang et al. 2012). However, difficulties have arisen in resolving variable stars within clusters due to the low angular resolution of ground-based telescopes, largely as a result of atmospheric effects.

The Panchromatic Hubble Andromeda Treasury (PHAT) survey is a multicycle HST program covering approximately one-third of M31’s disk and most of its bulge in six different wide-band filters, from the ultraviolet to near-infrared bands, at high resolution (J. J. Dalcanton et al. 2012; B. F. Williams & J. J. Dalcanton et al. 2014). More than 2000 stellar clusters have been identified in the PHAT survey data through the citizen-science Andromeda Project¹¹ (L. Clifton Johnson et al. 2015). These clusters are a rich arena for studying stars in rapid phases of their evolution, such as Cepheid variables. Few studies have been carried out thus far to probe stellar variability in extragalactic stellar clusters. For example, by cross-matching the Pan-STARRS1 Cepheid catalog of M. Kodric et al. (2013) with the PHAT cluster catalog, P. Senchyna et al. (2015)

identified potential Cepheids in M31 stellar clusters. However, a systematic study of variable stars in the PHAT clusters has not been done.

In this work, we perform a systematic search for variable stars in M31 clusters exclusively using the PHAT survey data. We constrain both the evolutionary phase and initial mass of our resulting cluster-variable stars via isochrone fitting. We structure the paper as follows. First, we describe the PHAT survey design and highlight its time-domain component in Section 2. We describe the methods used to identify the cluster-variable stars in Section 3, including the difference imaging (DI) pipeline. We present the results from the application of the DI pipeline and subsequent isochrone analysis of these variable stars in Section 4, along with an assessment of the effects of blending on our results. We describe the future direction of our study using the PHAT survey data in Section 5 before we summarize our findings in Section 6.

We have made the tables containing the properties of the variable stars, along with their light curves, accessible via a public directory on the NSF’s NOIRLab Astro Data Lab (M. J. Fitzpatrick et al. 2014) file storage system. A brief guide detailing how to access these data is provided in Appendix B.

2. Data

2.1. PHAT as a Time-domain Data Set

The HST imaging for the PHAT survey has been conducted using the Advanced Camera for Surveys (ACS) Wide Field Channel (WFC) and the Wide Field Camera 3 (WFC3) ultraviolet/optical (UVIS) and near-infrared (IR) channels, altogether providing coverage in six filters—F275W and F336W with WFC3/UVIS, F475W and F814W with ACS/WFC, and F110W and F160W with WFC3/IR (J. J. Dalcanton et al. 2012). The full survey area of 0.5 deg^2 is organized into 23 subareas called “bricks,” each spanning $\sim 6' \times 12'$, which are formed by 3×6 contiguous WFC3/IR pointings (or “fields”). Each brick is observed in two 3×3 halves taken 6 months apart by ACS/WFC. Due to the relatively large ACS/WFC field of view, its pointings contain overlapping regions, leading to multiple measurements of sources in those regions and thereby facilitating variability studies.

The photometric depth and spatial resolution (e.g., $\sim 0.''1$ for the F814W filter; J. Krist 2003) make PHAT ideal for studying resolved stellar populations in clusters. Of the six available filters, the optical F475W and F814W bands of ACS/WFC achieve the greatest optical depth (27.9 and 27.1 mag, respectively; J. J. Dalcanton et al. 2012). This, along with their repetition in the survey thanks to the survey tiling strategy mentioned above, make these filters the main source of data in our study. For each object detected in the PHAT survey in a given band, its *per-exposure* as well as *combined* (across exposures) photometric measurements have been obtained by B. F. Williams & J. J. Dalcanton et al. (2014) and B. F. Williams et al. (2018) using DOLPHOT (A. E. Dolphin 2000). The combined photometric measurements are generated by summing the corresponding pixel values of the exposures after scaling for the respective exposure times and removing the most deviant values (see A. E. Dolphin 2000 for details). The catalogs of both types of measurements are made available via the NOIRLab Astro Data Lab science platform (M. J. Fitzpatrick et al. 2014)—we use these catalogs for our study.

¹¹ <http://www.andromedaproject.org>

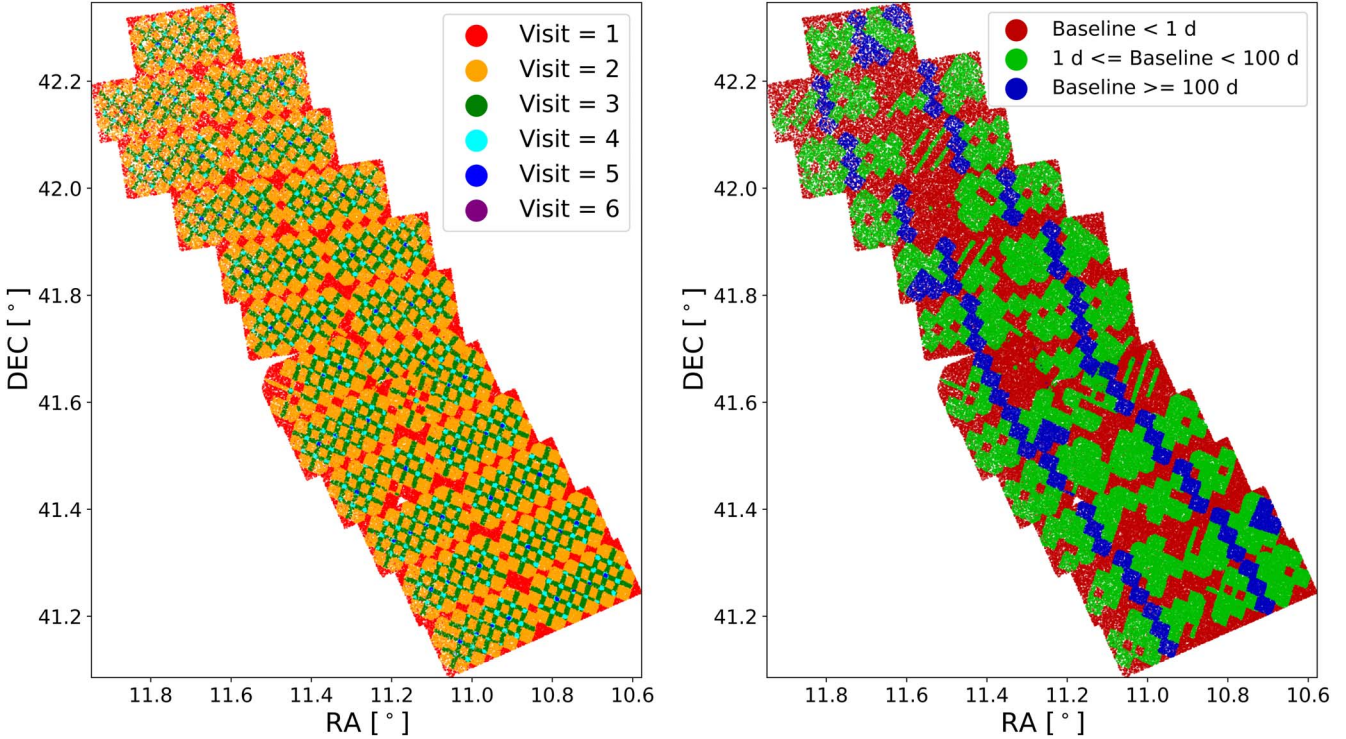


Figure 1. Left: map of the number of visits by ACS/WFC in the F814W filter to a representative sample of $\sim 200,000$ stars identified across the PHAT survey footprint. Right: map of the temporal baseline of all observations in the F814W filter for the same sample of stars. We obtain similar maps when using observations from the F475W filter.

Note that throughout this paper, we use the combined photometry for target selection and isochrone analysis, while the per-exposure photometry is used to construct light curves.

The left panel of Figure 1 displays a map of the number of visits made by ACS/WFC (F814W filter) to a representative sample of $\sim 200,000$ stellar sources identified in the PHAT footprint, showing that most sources have 1–3 visits each. Note that the ACS/WFC exposure map shown in Figure 5 of J. J. Dalcanton et al. (2012) roughly outlines a brick from this map. Each visit comprises a sequence of exposures. The temporal baseline—the time between first and last observations across all visits in F814W for a given source—over the PHAT footprint is also illustrated in the right panel of Figure 1. We observe that a majority of sources have a baseline that is < 1 day or 1–100 days.

2.2. PHAT Star Clusters

We use the list of 2753 clusters cataloged by L. Clifton Johnson et al. (2015) in our study and query for stars from the PHAT survey projected in each cluster. The clusters are distributed across the entire PHAT footprint, as shown in Figure 2. We identify candidate stars in each cluster using a search radius of $2 \times r_{\text{eff}}$, where r_{eff} is the half-light radius of the cluster as given in Table C1 of L. Clifton Johnson et al. (2015). We find a total of 294,981 stars within the identified PHAT clusters. Given the stellar crowding in these clusters, we only consider luminous stars, defined here as F814W magnitude < 19 mag, for our variability analysis, since at higher stellar densities the limiting magnitude is brighter for ACS data (L. C. Johnson et al. 2012). After applying this magnitude threshold, we obtain 376 luminous stars within 166 host clusters (see Table 1 for a summary of the number of stars identified at each step of our analysis).

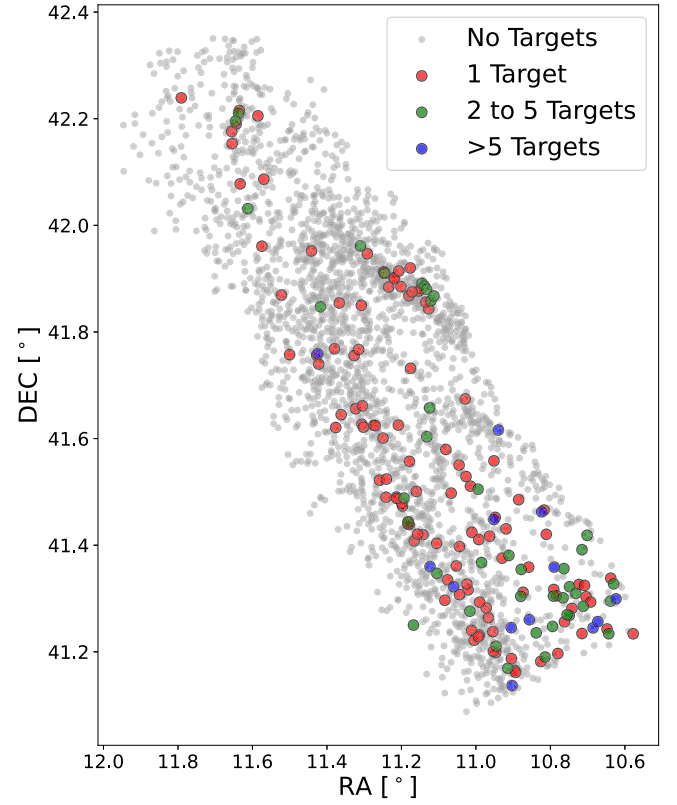


Figure 2. Distribution of the 2753 stellar clusters identified by L. Clifton Johnson et al. (2015) in the PHAT survey. Gray dots denote clusters excluded from our sample because they do not have any luminous ($F814W < 19$) stars. The remaining red, green, and blue circles indicate clusters with different numbers of luminous stars in our sample.

Table 1

Breakdown of the Number of Candidate Cluster-variable Stars Identified at Each Stage of the Vetting Process Described in Section 3

Criterion	Number of Stars
Full 2753 cluster sample	294,981
Star F814W < 19 mag	376
Number of exposures >1 (with $S^2 < 0.2$)	358
$\chi_{\text{red}}^2 > 2.5$	239
Number of visits > 1	212

Note. Values are calculated prior to application of the DI pipeline.

3. Method

We present our methods for identifying variable stars, beginning with an analysis of the F814W light curves of the 376 luminous cluster stars selected above to produce a list of stars with evidence of variability. We then use the per-visit images in F814W to confirm the variability of these stars via DI. We define the per-visit image of an object in a given filter as the image corresponding to a distinct brick-and-field combination obtained by combining all drizzled exposures at each observing epoch (visit). We download the per-visit ACS/WFC images used in this study from the Mikulski Archive for Space Telescopes (J. Dalcanton et al. 2012).

3.1. Light Curve: Calibration of Systematic Errors

The M31 stellar clusters are very crowded fields with median $r_{\text{eff}} \sim 0.^{\circ}44$ (L. C. Johnson et al. 2012). The HST photometry of stars within these clusters might therefore be contaminated due to crowding effects, and, subsequently, the reported measurement errors may be underestimated. We account for this by applying a magnitude-dependent correction to the measurement errors of the per-exposure photometry values retrieved from the Astro Data Lab catalog (K. Olsen et al. 2018; B. F. Williams et al. 2018). We refer to this correction as systematic error calibration. We obtain this quantity by considering a sample of PHAT survey stars within M31 stellar clusters that have temporal baselines shorter than 1 day and are brighter than 19 mag in the F814W filter. We manually inspect the per-visit F475W and F814W filter images for each of these sources, discarding sources with images visibly affected by bad pixels to prevent introducing errors into our calibration. We reach a sample size of 129 stars after applying these cuts. We then calculate the mean magnitude and standard deviation (σ) of the F814W light curve for each of these sources after removing any measurements affected by cosmic-ray strikes, bad pixels, etc. by thresholding on the sharpness (S) stellar profile statistic available in the catalog.¹² The sharpness value is close to zero for a starlike profile; we use a threshold of $S^2 < 0.2$ (see also B. F. Williams & J. J. Dalcanton et al. 2014).

The left panel of Figure 3 shows the standard deviation versus mean magnitude for these 129 cluster stars. The right panel of the figure shows the F475W – F814W color versus F814W magnitude for these stars, along with a heat map produced using the B. F. Williams & J. J. Dalcanton et al. (2014) catalog of more than 117 million M31 stars identified throughout the PHAT survey. The marker colors for each cluster star plotted in Figure 3 are based on the distinctive

plumes of stars visible at F814W $\lesssim 19$ mag, denoting redder stars at/above the tip of the RGB ($F475W - F814W \geq 2.3$), intermediate-color stars ($1 \leq F475W - F814W < 2.3$), and bluer stars ($F475W - F814W < 1$). We find a clear bimodal distribution of light-curve standard deviations of all the cluster stars in our calibration sample, as shown in the left panel of Figure 3. This sample of stars therefore comprises two broad groups with σ above or below ~ 0.05 mag: the group with higher values predominantly composed of stars with intermediate colors ($1 \leq F475W - F814W < 2.3$) compared with the other group, which contains the majority of the redder ($F475W - F814W \geq 2.3$) and bluer ($F475W - F814W < 1$) stars in the sample. Red variable stars are known to have characteristic timescales of a few hundred days (e.g., M. D. Soraisam et al. 2020), so it is significant that the majority (90%) of the redder stars in our calibration sample with short (<1 day) time baseline light curves have $\sigma < 0.05$ mag, placing them in the lower of the two bimodal groups. We therefore make the assumption that the group of stars with $\sigma < 0.05$ mag are nonvariable based on the available PHAT survey data, their measured variations instead being dominated by noise.

We use all the stars in this lower group to calibrate the systematic error as follows. For each star in this group, we use the standard deviation of its light curve as an estimate of the error on its F814W magnitude measurement (σ_m). We place the stars into four magnitude bins according to their mean light-curve magnitudes and compute the average σ_m within each bin ($\bar{\sigma}_m$). We then determine the optimal systematic error to add to the reported error of all data points in the magnitude bin by identifying the correction value that minimizes the square difference between $\bar{\sigma}_m$ and σ for data points in that bin. The systematic errors of the 376 luminous cluster stars are then calibrated by grouping the stars into the same magnitude bins identified for the calibration sample and applying the systematic error values to the stars in each bin.

3.2. Light Curve: Reduced χ^2 Analysis

After calibrating the systematic error for our sample of 376 stars, we analyze their F814W light curves for photometric variability. We identify and exclude any star with only a single exposure in its F814W light curve and also exclude measurements of the stars with sharpness parameter $S^2 \geq 0.2$ as described above, which leaves 358 stars. We then investigate the light curves for these remaining 358 stars by comparing each F814W observation to its mean light-curve value using reduced chi-squared, χ_{red}^2 , as a metric. The left panel of Figure 4 shows the χ_{red}^2 versus the temporal baseline of the F814W light curve for these stars. As can be seen, the stars in our sample occupy the full χ_{red}^2 –baseline space and many have $\chi_{\text{red}}^2 > 1$ over the full range of baselines, indicating potential variability in their F814W light curves. In contrast, when the same χ_{red}^2 -versus-baseline analysis is performed for classified field Cepheids from R. Wagner-Kaiser et al. (2015) using their PHAT F814W light curves, shown in the right panel of Figure 4, there is a clear increase to $\chi_{\text{red}}^2 > 2.5$ at baselines >1 day. This is concurrent with the known variability periods of classical Cepheids of ~ 1 –100 days, indicating that the PHAT light curves are capturing the variability of these stars. We therefore apply a threshold of $\chi_{\text{red}}^2 > 2.5$ to our sample of 358 stars to select those with light curves showing evidence of

¹² Note that this sharpness parameter is distinct from that described later in this work.

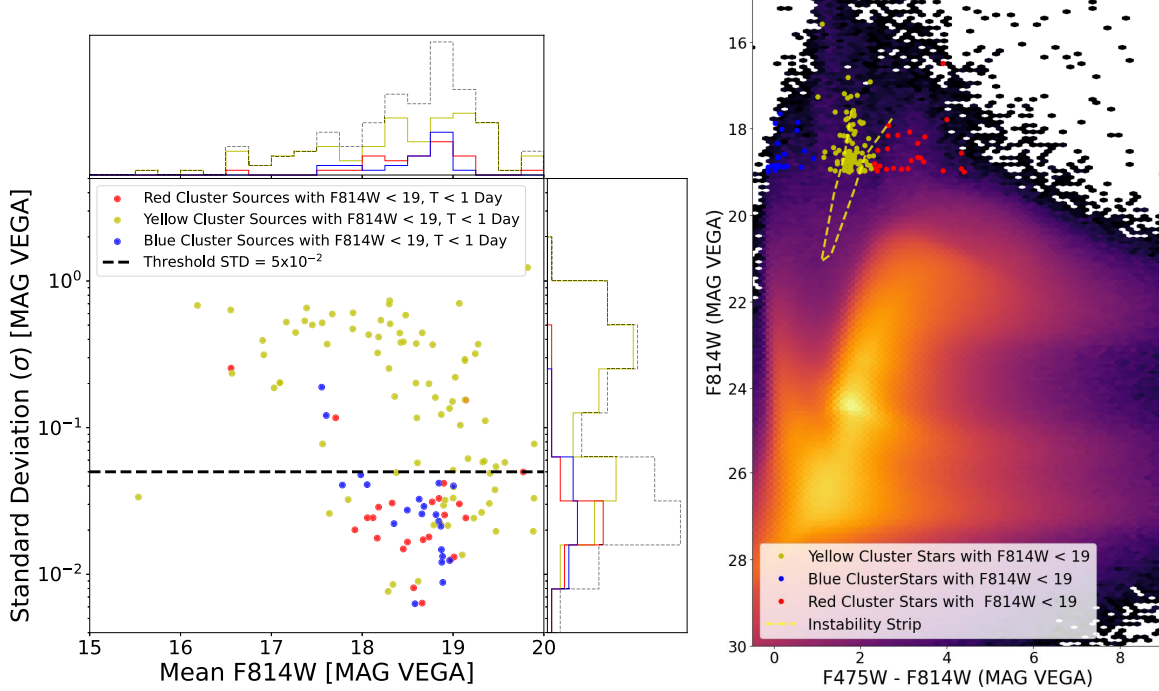


Figure 3. Left: mean vs. standard deviation of the light curves of luminous (combined F814W magnitude < 19) cluster stars with temporal baselines < 1 day. As opposed to the combined magnitudes used to filter the luminous stars, the mean magnitudes on the x-axis are simple (i.e., unweighted) means of the light curves after applying a conservative threshold of a sharpness-squared value less than 0.2 (see Section 2.1). Right: color–magnitude diagram for the same luminous cluster stars. They are separated into blue, yellow and red cluster stars based on their F475W – F814W color positions on the CMD (see text for details). The background heat map is generated using the B. F. Williams & J. J. Dalcanton et al. (2014) catalog of M31 stars. The yellow dashed line indicates the theoretical Cepheid instability strip from G. Fiorentino et al. (2002) for $Z = 0.02$, using a distance modulus of 24.47 (A. W. McConnachie et al. 2005) and applying a foreground extinction of $A_V = 0.19$ (using the foreground reddening of $E(B - V) = 0.06$ along the line of sight to M31; M. A. Cordner et al. 2011). We use stars with standard deviations $\lesssim 0.05$ mag to calibrate the systematic error, chosen based on the distribution of standard deviations for presumed nonvariable redder stars in the sample.

variability in PHAT observations. This results in 239 candidate cluster-variable stars.

3.3. Vetting of Per-visit Images

We visually examine the per-visit images of each of the 239 candidate cluster-variable stars identified above to investigate the behavior and source of the detected variability at each HST visit. We aim to identify variability caused by contaminants, such as cosmic-ray strikes on the detector, as these contaminants will result in inaccurate variability measurements for the affected candidate cluster-variable stars. This process revealed that a large fraction of the per-visit images are affected by cosmic-ray strikes. However, the manual examination of the images around the candidate cluster-variable stars proved to be a much greater challenge due to the lack of contrast in the crowded cluster environments. We therefore turned to using a more robust method—DI—to efficiently validate our sample of candidate cluster-variable stars.

In order to carry out the DI analysis of a source, at least one pair of per-visit images is needed. We assess the available data of the 239 candidate variable stars to find those with more than one HST visit. We use the per-exposure photometry catalog from Astro Data Lab (K. Olsen et al. 2018; B. F. Williams et al. 2018) to identify unique observing epochs for each candidate variable star. Following this step, the number of candidate cluster-variable stars that could be processed using the DI pipeline is reduced to 212. Table 2 details the properties of each

of the final 212 candidate cluster-variable stars prior to the application of the DI pipeline.

3.4. Difference Imaging Pipeline

We verify the potential variability detected in the light curves of our 212 candidate cluster-variable stars by developing and applying a DI pipeline to their available F814W per-visit images. Performing DI analysis only between images with the largest difference in light-curve magnitudes may limit the potential number of confirmed variables if at least one of the frames is affected by contaminants such as cosmic-ray strikes, bad detector columns, etc. We therefore choose to use all the images covered by the F814W light curve of a given candidate variable star, differencing the first available visit image (which we refer to as the *template frame*) and all subsequent visit images (*science frames*).

As a given M31 stellar cluster may host multiple candidate cluster-variable stars, we generate 250 pixel \times 250 pixel (12''.5 \times 12''.5) cutouts from the visit images centered on the L. Clifton Johnson et al. (2015) coordinates of each host cluster to be used as template and science frames. This cutout size also ensures that there are at least 20 bright stars around the cluster in both frames. This is critical, as we use these noncluster stars in image alignment and point-spread function (PSF) matching, as described in the following sections. Furthermore, using these cutouts minimizes the effects of ACS/WFC detector geometric distortion (J. E. Ryon 2023) and the spatial variation of the

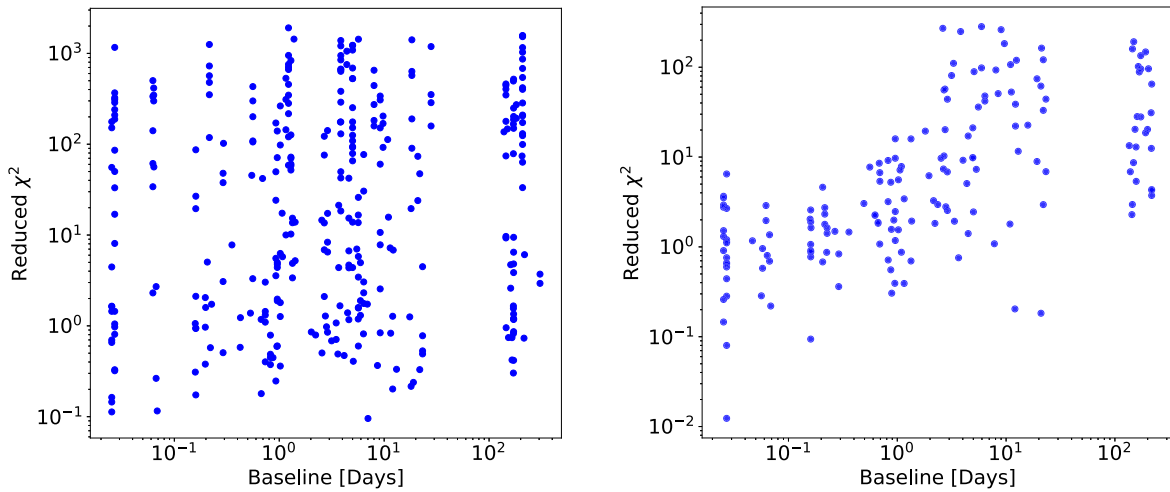


Figure 4. Left: χ^2_{red} vs. temporal baseline for the 358 luminous ($F814W < 19$) cluster stars with more than one exposure identified in the PHAT data (see Section 2.2). Right: χ^2_{red} vs. temporal baseline for classified field Cepheids from R. Wagner-Kaiser et al. (2015).

ACS/WFC PSF (J. Krist 2003) while also including sufficient image background for accurate background flux measurements.

3.4.1. Bad-pixel Mask, Image Alignment, and Background Matching

We create a bad-pixel mask for each pair of template and science frames for a given candidate variable star host cluster. Starting with an empty array with the same dimensions as the science and template cutout frames as the basis for our mask array, we identify pixels with nonphysical values (i.e., nonpositive values, as the pixel values are in units of electron s^{-1}) in either the template or science frame and add them to the mask array. We then mask the surrounding ± 5 pixels around each of these pixels in order to exclude potential lower-level effects unaccounted for in image processing. We apply this bad-pixel mask to both science and template frames in the pair, repeating the above process for each of the template–science frame pairs for the host cluster.

Once masked, we transform the frames for a given host cluster onto the same coordinate plane by reprojecting each science frame onto the template frame using the `reproject` library from `astropy` and their respective World Coordinate System (WCS) header information. We then ensure subpixel alignment between the template and science frames using `astroalign` (M. Beroiz et al. 2020a), which estimates the affine transformation between the two frames by matching asterisms in the frames.

Background matching of each pair of aligned-science and template frames is performed by first subtracting the template frame from the former to produce an intermediate difference image. We then use `Background2D` from the `photutils` package (L. Bradley et al. 2023) to generate a 2D background map from the intermediate difference image. The `boxsize` and `filtersize` parameters of `Background2D` are adjusted manually for each pair of frames on a case-by-case basis through multiple iterations to optimize the background estimation by checking for any abnormal behavior in the 2D map (under- or oversmoothing of the image background and cluster residuals). We find that a `boxsize` of 10 and `filtersize` of 5 are generally applicable to avoid creating large “dipoles”—immediately adjacent hemispheres of significant over- and undersubtraction caused by oversmoothing of local maxima—in the intermediate difference images. The

resulting 2D background map is then added to the template frame.

3.4.2. PSF Matching

To assess the quality of the observed PSF in each pair of science and template frames, we identify a matching set of bright stars away from the bright cluster core using `DAOSTarFinder` in `photutils` (L. Bradley et al. 2023). To this end, we filter bright stars in each frame with magnitudes $>5\sigma$ (standard deviation) above the median magnitude of all stars in the frame. We then apply a cut based on radial distance from the image center to only consider sources in the outer 20th percentile of the frame. We cross-match the identified stars from the template and aligned science frame to keep those detected in both frames.

The observed PSF of each matched star is then modeled as a 2D Gaussian using `Gaussian2D` from `astropy`. The full width at half-maximum (FWHM) of the model PSF minor axis is used as a zeroth-order estimate of the resolution, since it provides a more consistent estimate in the case of PSF elongation along one axis due to blending of stars. We apply sigma clipping to the distribution of model PSF FWHMs to exclude sources with poor model fits. We then compare the mean FWHM value for all bright matching stars between the science and template frames. The frame with the smaller value (i.e., higher resolution) is convolved with a kernel generated using the adaptive Bramich routine (J. P. Miller et al. 2008) of the optimal image subtraction (OIS) library (M. Beroiz et al. 2020b) to match the PSF between the pair of science and template frames. To prevent the bright, crowded core region of the cluster from adversely affecting the OIS kernel construction, we incorporate an optional mask covering the cluster core into the OIS software. Applied only during construction of the convolution kernel, the size of this additional square-shaped cluster mask is manually varied between 1 and 15 pixels along each axis depending on the radial extent of the cluster in each frame. Once the convolution kernel is applied, the convolved frame is subtracted from the less-resolved frame to produce the difference image for the two per-visit frames of the given host cluster.

Table 2
Candidate Variable Stars Identified in M31 Clusters through the Vetting Process Described in Section 3

Cluster ID	Cluster R.A. (deg)	Cluster Decl. (deg)	PHAT ID	PHAT R.A (deg)	PHAT Decl. (deg)
27	11.016225	41.276218	PHAT_11.0161713+41.276141	11.016171	41.276141
91	10.990885	41.231335	PHAT_10.9906814+41.231282	10.990681	41.231282
93	11.011452	41.240176	PHAT_11.0114911+41.240166	11.011491	41.240166
230	11.127033	41.843671	PHAT_11.1262019+41.843634	11.126202	41.843634
285	10.945997	41.210538	PHAT_10.9464478+41.209956	10.946448	41.209956
390	10.911579	41.380726	PHAT_10.9115373+41.380738	10.911537	41.380738
403	11.104662	41.347108	PHAT_11.1047292+41.346899	11.104729	41.346899
403	11.104662	41.347108	PHAT_11.1046035+41.347157	11.104603	41.347157
403	11.104662	41.347108	PHAT_11.1050349+41.347152	11.105035	41.347152
445	10.951771	41.448099	PHAT_10.9517399+41.448030	10.951740	41.448030
445	10.951771	41.448099	PHAT_10.9516719+41.448098	10.951672	41.448098

Note. We use the same cluster IDs as in L. Clifton Johnson et al. (2015).

(This table is available in its entirety in machine-readable form in the [online article](#).)

The general DI procedure described above can be summarized as

$$D = I - (R \otimes K), \quad (1)$$

where I is the less-resolved frame, R is the higher resolution frame, K is the convolution kernel determined from the OIS Bramich routine, and D is the difference image. We apply these steps to all visit-image pairs of the 212 candidate variable star host clusters to obtain clean DI frames with minimal artifacts.

3.4.3. DI Source Detection

To confirm the variability of each of our 212 candidate variable stars, we identify significant residuals (at the location of the star) in the difference images produced for each star. We first obtain an estimate of the local background in a circular annulus around the host cluster. We set the inner and outer radii of the annulus based on the $0.^{\prime\prime}11$ FWHM of the ACS instrument (e.g., M. Santiago-Cortés et al. 2010), using an inner radius of $10 \times$ FWHM and outer radius of $20 \times$ FWHM to include the local background of the cluster without including candidate cluster-variable stars. We then use the mean of the pixel values within the annulus area as the estimate of the local background.

We next use the DAOStarFinder routine of photutils to detect sources at 5σ above the local background in the difference images. Any detections within a $0.^{\prime\prime}11$ radius of a candidate variable star position in the difference image are designated as potential counterparts to that candidate variable star. If no detections are found in this first pass, the image is inverted and the DAOStarFinder search repeated to allow for negative residuals to be detected. Candidate cluster-variable stars with no corresponding sources within a $0.^{\prime\prime}11$ radius of their position in all of their host cluster difference images are excluded from further analysis. From our sample of 212 candidate cluster-variable stars, we identify counterpart difference image sources for 89 stars using this DAOStarFinder source search, confirming their variable nature.

We now use the DAOStarFinder¹³ sharpness, peak, and flux output parameters for the source detection(s) associated with each confirmed variable star as metrics to

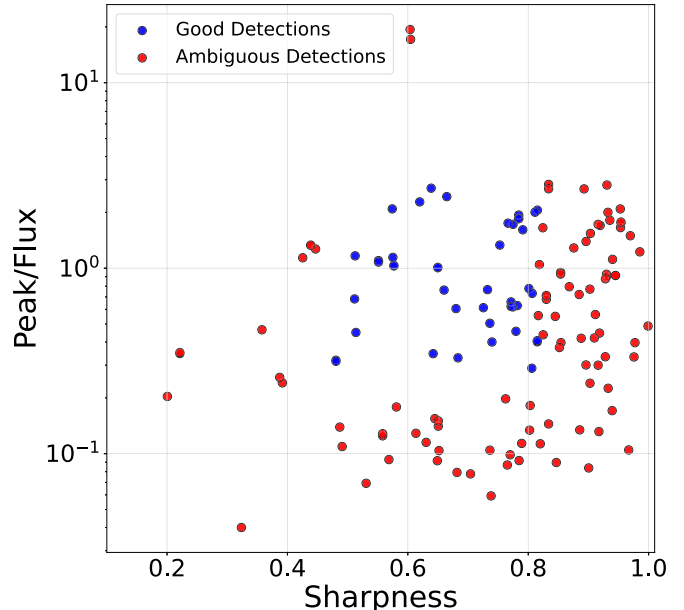


Figure 5. Sharpness vs. peak/flux parameter values from DAOStarFinder for all sources detected within a $0.^{\prime\prime}11$ radius of a candidate cluster-variable star position across all host cluster difference images, divided into *Good* and *Ambiguous* categories as described in Section 3.4.3.

categorize the source detection(s) into one of two groups based on the source exhibiting stellar-like behavior (“*Good*”) or not (“*Ambiguous*”), e.g., due to potential contamination by DI artifacts. We determine *Good* source detections to be those with $0.26 < \text{peak/flux} < 10.84$ (between the 30th and 99th percentiles) and $0.48 < \text{sharpness} < 0.82$ (between the 9th and 59th percentiles) when considering the DAOStarFinder parameters of all the detections associated with cluster-variable stars, as shown in Figure 5. Source detections with one or both metrics outside these ranges are classified as *Ambiguous*. Any candidate cluster-variable star with at least one *Good* detected source is then designated as having *Good* (stellar-like) difference image source detection behavior; otherwise, the star is deemed to have *Ambiguous* source detection behavior.

Examples of template, science, and difference image frames for *Good* and *Ambiguous* detection classifications are shown in Figures 6 and 7, respectively, with light curves for the corresponding cluster-variable star candidates shown in

¹³ <https://photutils.readthedocs.io/en/stable/api/photutils.detection.DAOStarFinder.html>

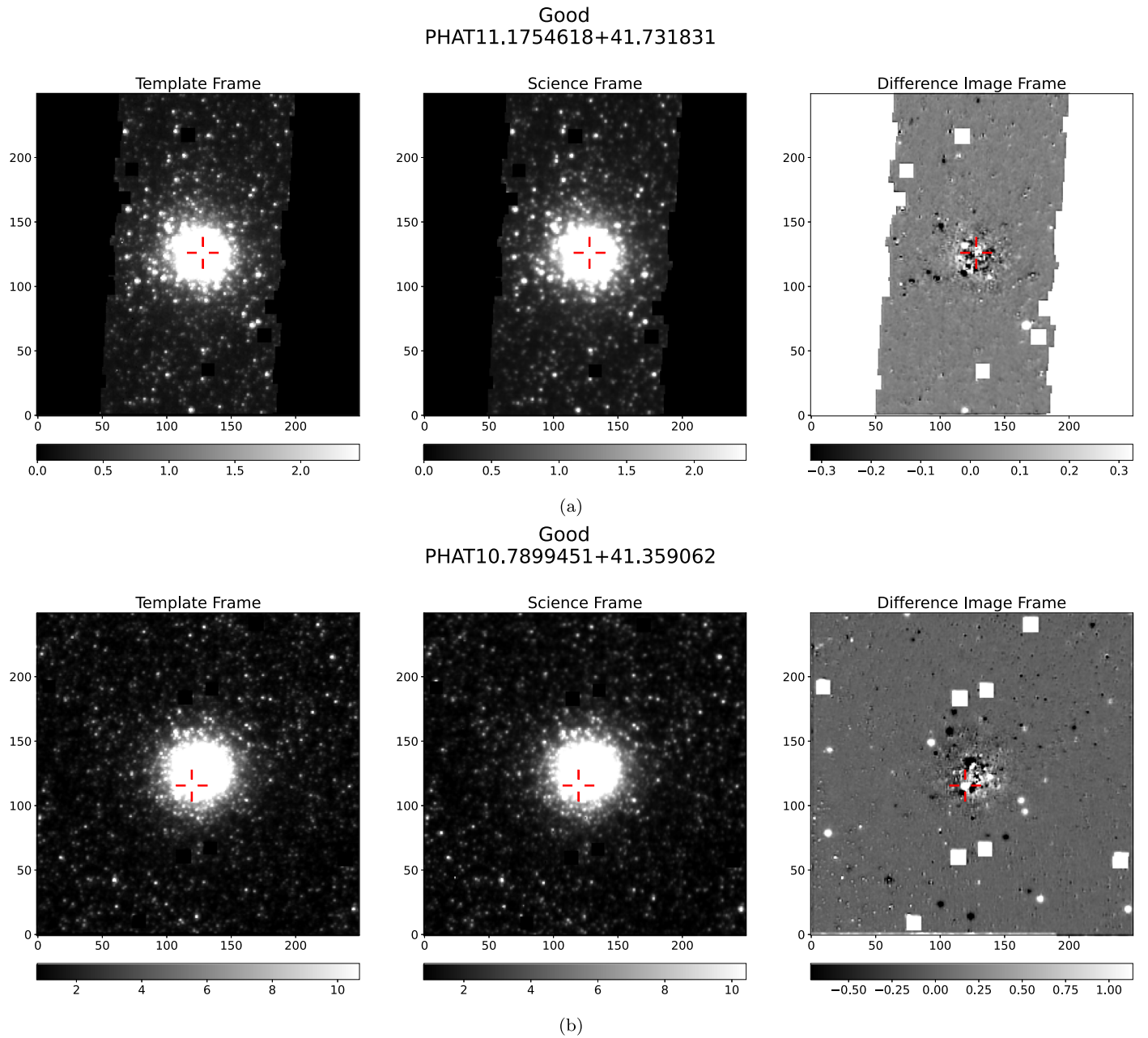


Figure 6. Examples of *Good* cluster-variable star source detections as described in Section 3.4.3, with the difference image being the science minus template frame. The red crosshair in each frame indicates the location of the detection.

Figures 8 and 9. After applying the DI pipeline to the 212 variable star candidates and performing the subsequent source detection analysis, we are able to confirm 89 cluster-variable stars in 50 host clusters. Of these, we find 38 stars with at least one *Good* source detection and 51 stars with *Ambiguous* source detections based on the thresholds outlined above.

3.5. Chance Coincidence with Field Stars

Before analyzing the 89 cluster-variable stars further, it is prudent to assess the potential of contamination of our sample by luminous field stars. To do this, we first identify the number of bright ($F814W < 19$) field stars detected across the entire PHAT survey footprint, finding a total of 7635 stars. By making the simplifying assumption that these field stars are uniformly distributed across the PHAT survey area, we are able

to obtain a stellar density of $\approx 1.22 \times 10^{-3}$ arcsec $^{-2}$ for these bright stars. Based on the radii of each of the M31 stellar clusters tabulated in the L. Clifton Johnson et al. (2015) catalog, we find the total area of the 2753 clusters to be ≈ 3260 arcsec 2 . The expected number of luminous field stars appearing in these clusters by chance is then ≈ 4 . Using Poisson statistics, we find a negligible (close to zero) probability of randomly finding 89 or more luminous field stars in the clusters; the probability of finding more than nine of such field stars in clusters by chance is less than 1%. We therefore conclude that it is highly unlikely that the majority of the luminous cluster-variable stars we have identified are contaminant field stars.

Nevertheless, we cannot rule out that a small fraction of these stars are in fact field stars. To investigate this possibility, we search for potential foreground stars in our sample of 89 cluster-variable stars using available Gaia DR3 data accessible

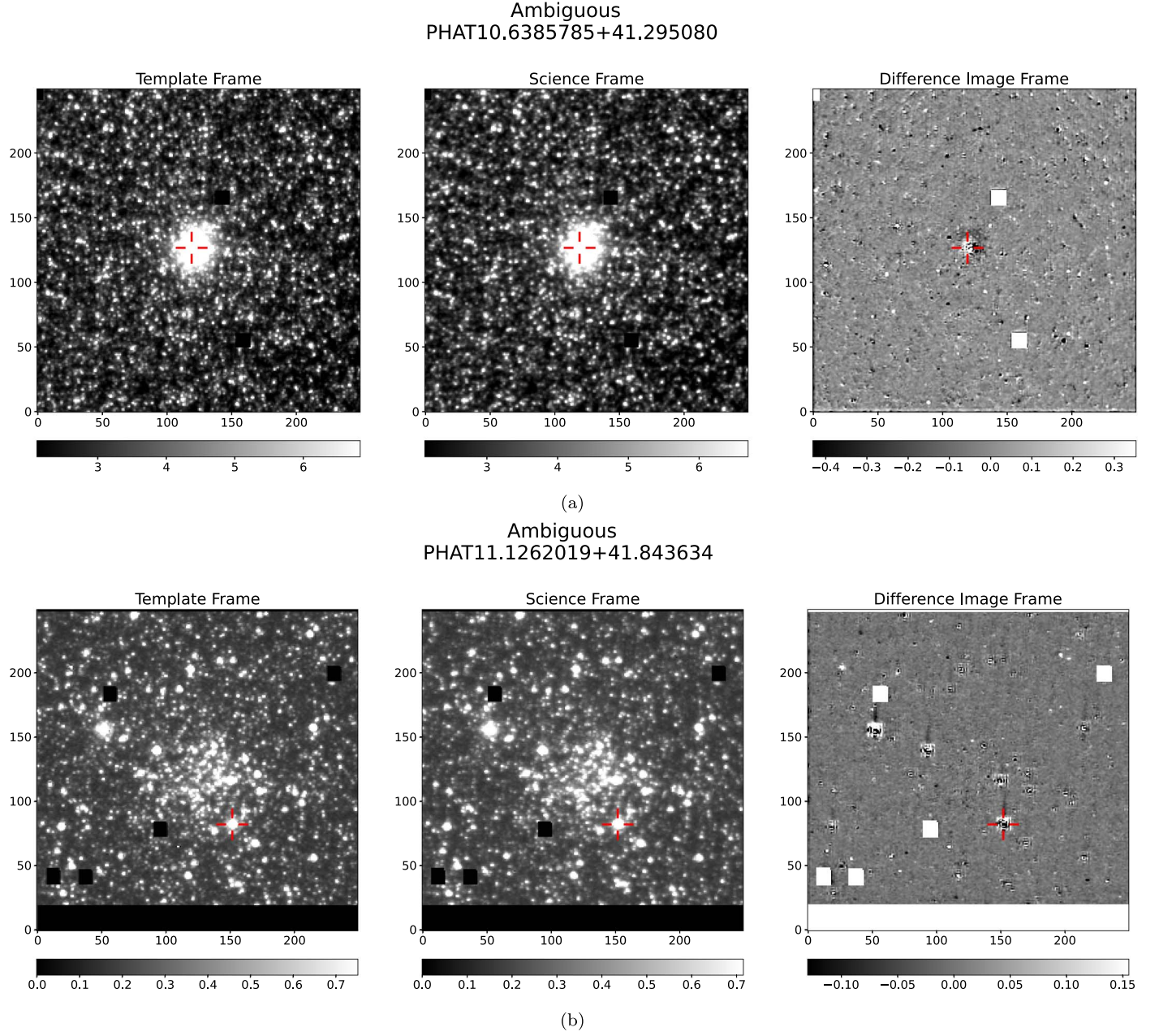


Figure 7. Examples of *Ambiguous* cluster-variable star source detections as described in Section 3.4.3, with the difference image being the science minus template frame. The red crosshair indicates the location of the detection.

through Astro Data Lab and the method of P. Barmby (2023; see Appendix D for details). We find three likely foreground stars, which leaves a final sample of 86 confirmed cluster-variable stars in 47 host clusters, of which 37 stars have at least one *Good* source detection and 49 stars have *Ambiguous* source detections, as described above.

4. Results

We have identified 86 cluster-variable stars in 47 host clusters through the application of our DI pipeline. We now proceed to infer the evolutionary phases and initial masses of these stars by matching each star to the most probable point on an isochrone generated using the derived properties of the host cluster. We also consider the blending effects on the PHAT photometry, using representative samples of likely and less

likely to be blended stars in the PHAT clusters to calculate the probability of each cluster-variable star in our sample being blended based on their available properties. We then use the inferred fundamental parameters of the stars to classify the type of variability, qualified by the source detection behavior and blending probability of each cluster-variable star.

4.1. Isochrone Generation

We use the MESA Isochrones and Stellar Tracks (MIST; J. Choi et al. 2016; A. Dotter 2016) web interpolator¹⁴ to generate an isochrone for each variable-star-hosting cluster. To do this, we use estimates of age, extinction (A_V) and metallicity for the PHAT clusters provided by P. de Meulenaer et al.

¹⁴ https://waps.cfa.harvard.edu/MIST/interp_isos.html

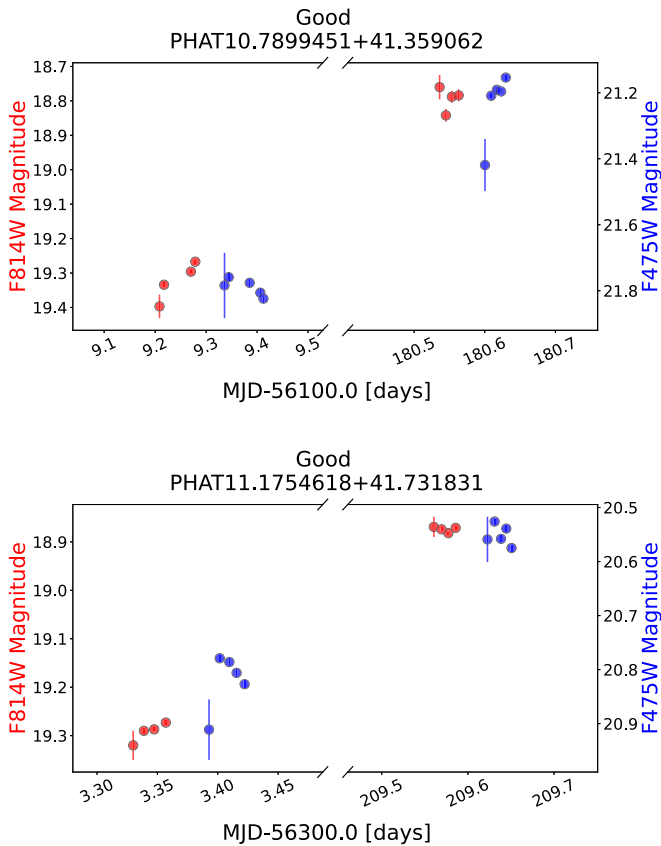


Figure 8. F814W and F475W light curves for the two example *Good* cluster-variable stars shown in Figure 6.

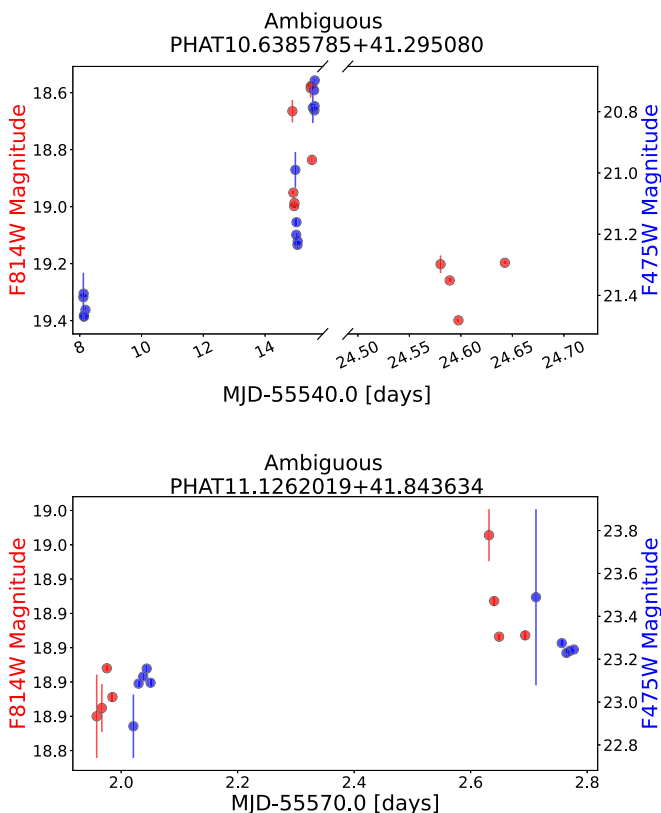


Figure 9. F814W and F475W light curves for the two example *Ambiguous* cluster-variable stars shown in Figure 7.

(2017), which they obtain by comparing the integrated broadband photometry of a given cluster with a 4D grid of models parameterized by cluster age, mass, extinction, and metallicity (P. de Meulenaer et al. 2015, 2017, and references therein). In their analysis of the derived metallicities, P. de Meulenaer et al. (2017) show that there is a high prevalence of solar or supersolar metallicity values in younger (<1 Gyr) stellar clusters, while older (≥ 1 Gyr) clusters exhibit a broader metallicity distribution. This motivates keeping the metallicity of younger (<1 Gyr) clusters fixed to a solar value ($Z = 0.02$) while allowing the metallicity of older clusters to vary. These authors also show that there is reasonable agreement between their results and those of N. Caldwell et al. (2011), which are based on spectroscopic observations, for the age, mass, and metallicity of the clusters common to both studies, barring extinction (see P. de Meulenaer et al. 2017).

We adopt the P. de Meulenaer et al. (2017) properties derived with nonsolar metallicity if its resulting age estimate is >1 Gyr and otherwise select the properties derived using solar metallicity. The selected age and metallicity values for each host cluster are used to generate an extinction-free MIST isochrone for that cluster. Stellar rotation is known to play an important role in stellar evolution (e.g., G. Meynet & A. Maeder 2000; R. Hirschi et al. 2004). We assume that rotation takes place, but with a moderate effect on the evolutionary tracks, by adopting a velocity ratio of $v_{\text{initial}}/v_{\text{critical}} = 0.4$ (J. Choi et al. 2016, and references therein).

We transform the A_V estimate of the given cluster derived by P. de Meulenaer et al. (2017) to the appropriate wavelength-dependent extinction for the PHAT bands, A_λ , using the conversion factors from Y. Wang et al. (2022; 1.17 for F475W, 0.65 for F814W) and apply it to the observed magnitudes of each variable star in the cluster to correct for extinction. We adopt a distance modulus of 24.47 for M31 (A. W. McConnachie et al. 2005) to convert the apparent magnitudes of the variable stars into absolute magnitudes.

4.2. Isochrone Matching

We use the generated isochrone of each host cluster to obtain the most likely properties for each of our variable stars using a modified version of the Bayesian method presented by L. da Silva et al. (2006). We calculate a posterior probability for each datum along the host cluster isochrone given the observed color and magnitude properties of the star following

$$P(M'_{\text{init}}) \propto \phi(M'_{\text{init}}) \exp \left[-\frac{(x - x')^2}{\sigma_x^2} - \frac{(y - y')^2}{\sigma_y^2} \right], \quad (2)$$

where we use a Salpeter (E. E. Salpeter 1955) initial mass function (IMF) $\phi(M'_{\text{init}})$ as the prior for the initial stellar mass of the isochrone datum, M'_{init} ; x and y are the observed F475W – F814W color and F814W absolute magnitude of the variable star, respectively; x' and y' are the corresponding theoretical F475W – F814W color and F814W absolute magnitude for the isochrone datum, respectively.

We estimate the variance of the observed properties, σ_x^2 and σ_y^2 in Equation (2), by first considering that the positions of our cluster-variable stars on the CMD are unlikely to represent their equilibrium states based on the sparsely sampled PHAT measurements. To facilitate the matching of our variable stars to their host cluster isochrones, we construct error ellipses

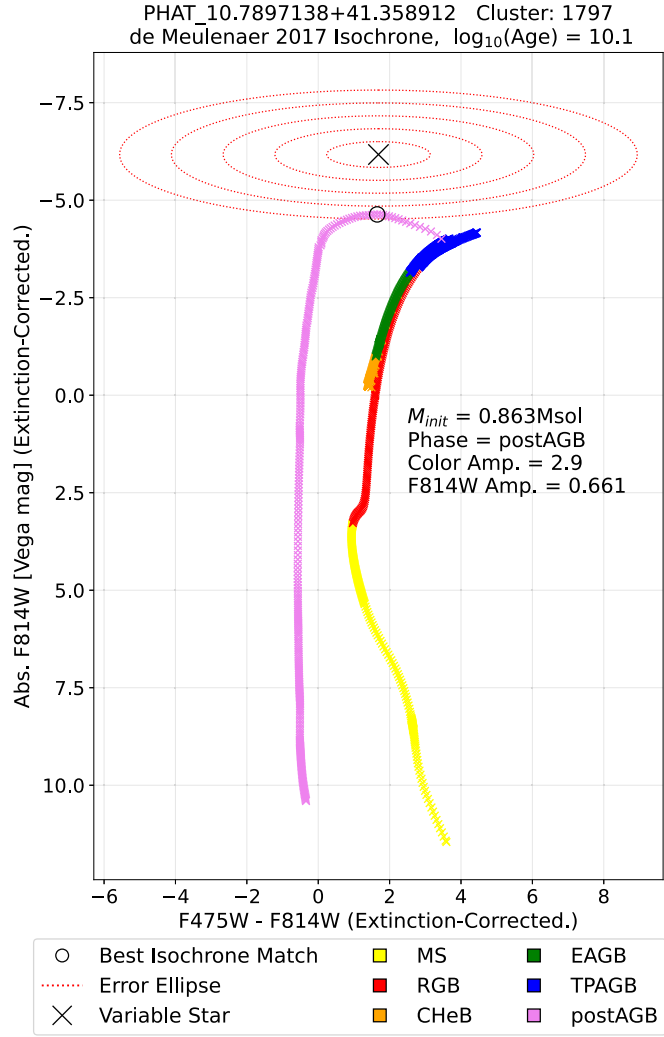


Figure 10. An example F475W – F814W vs. F814W absolute magnitude CMD showing how the error ellipse of the variable star is scaled to intersect with the host cluster isochrone.

using estimates of their observed amplitudes in F814W magnitude and F475W – F814W color space. For each variable star, we compute the largest difference between measurements comprising its F814W light curve (Δm_{F814W}) and adopt it as the radius along the vertical axis of its error ellipse. Note that Δm_{F814W} provides only a lower bound to the light-curve amplitude of each star in our sample, since the sparse PHAT observations may not cover the full extent of their light curves. We further estimate the color amplitude ($\Delta c_{\text{F475W},\text{F814W}}$) of each variable star in our sample by identifying the pair of F475W and F814W measurements from its corresponding light curves that produce the largest color value. This $\Delta c_{\text{F475W},\text{F814W}}$ value is used as the radius along the horizontal axis of its error ellipse. We then place the error ellipse on a CMD, centered on the variable star, along with its host cluster isochrone and scale the size of the ellipse until it intersects or surpasses one or more points on the isochrone. We use these scaled error values as estimates of the variance on each observed parameter in Equation (2). Figure 10 shows an example F475W – F814W versus F814W absolute magnitude CMD for a variable star in our sample, demonstrating the scaling of its error ellipse until it intersects with its host cluster isochrone.

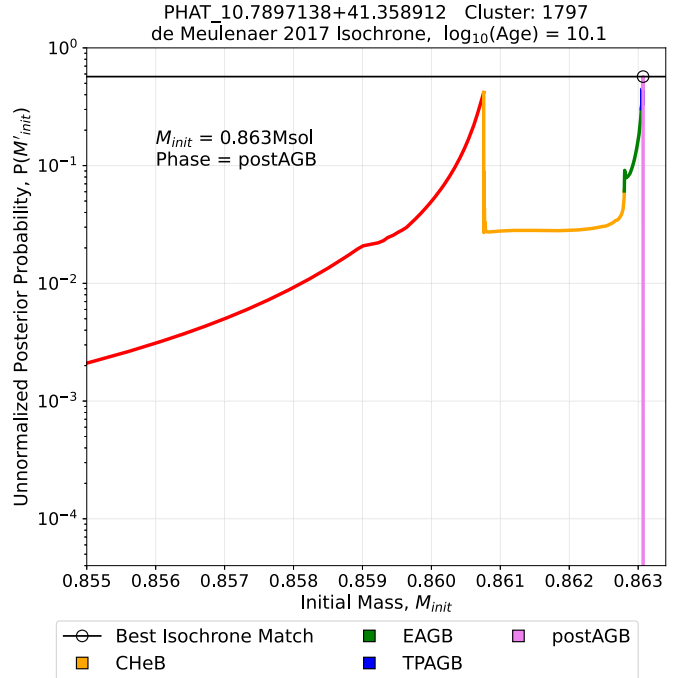


Figure 11. Posterior probability distribution of initial mass for the variable star shown in Figure 10, demonstrating the narrow initial mass range over which the post-MS evolution occurs for the older ($\gtrsim 1$ Gyr) isochrones. In such cases, the posterior probability is driven by the likelihood (see Section 4.2).

After computing the posterior probability distribution for a given cluster-variable star using Equation (2), we identify the maximum a posteriori isochrone datum and adopt its initial stellar mass and evolutionary phase to be those of the variable star. Figure 11 shows the unnormalized posterior distribution for the same cluster-variable star in Figure 10. The distribution shown in Figure 11 is typical of the distributions produced for the older ($\gtrsim 1$ Gyr), highly evolved variable stars in our sample. The post-MS evolution for their host cluster isochrones occurs over a narrow range of initial masses ($< 0.33 M_{\odot}$). This leads to a near-negligible effect from the IMF prior, the posterior probability instead being driven by the magnitude- and color-dependent likelihood term in Equation (2). In such cases, the most probable datum on the isochrone ends up being the point closest to the variable star in color–magnitude space. Hence, despite the longer lifetimes of the early asymptotic giant branch (EAGB) and thermally pulsing asymptotic giant branch (TPAGB) phases, we obtain the post-asymptotic giant branch (post-AGB) phase as the most probable result for the variable star in Figure 11 since it is closest to the datum with that phase (Figure 10); see, however, the caveats in Section 4.5.

It is also prudent to investigate how varying host cluster properties (age, metallicity and extinction) as well as distance modulus within their measured uncertainties affect the resulting isochrone matches. However, formal uncertainties are not available for the host cluster properties measured by P. de Meulenaer et al. (2017). As noted above and in their Figure 9, P. de Meulenaer et al. (2017) highlight the consistency between their cluster metallicity values and those of N. Caldwell et al. (2011) for clusters common to both studies. We use this consistency to identify a single cluster—number 3801 (Johnson et al. cluster ID)—with metallicity measurements in both studies consistent with the $Z \sim 0.02$ modal value of the 47 confirmed variable star host clusters in our sample. We then use

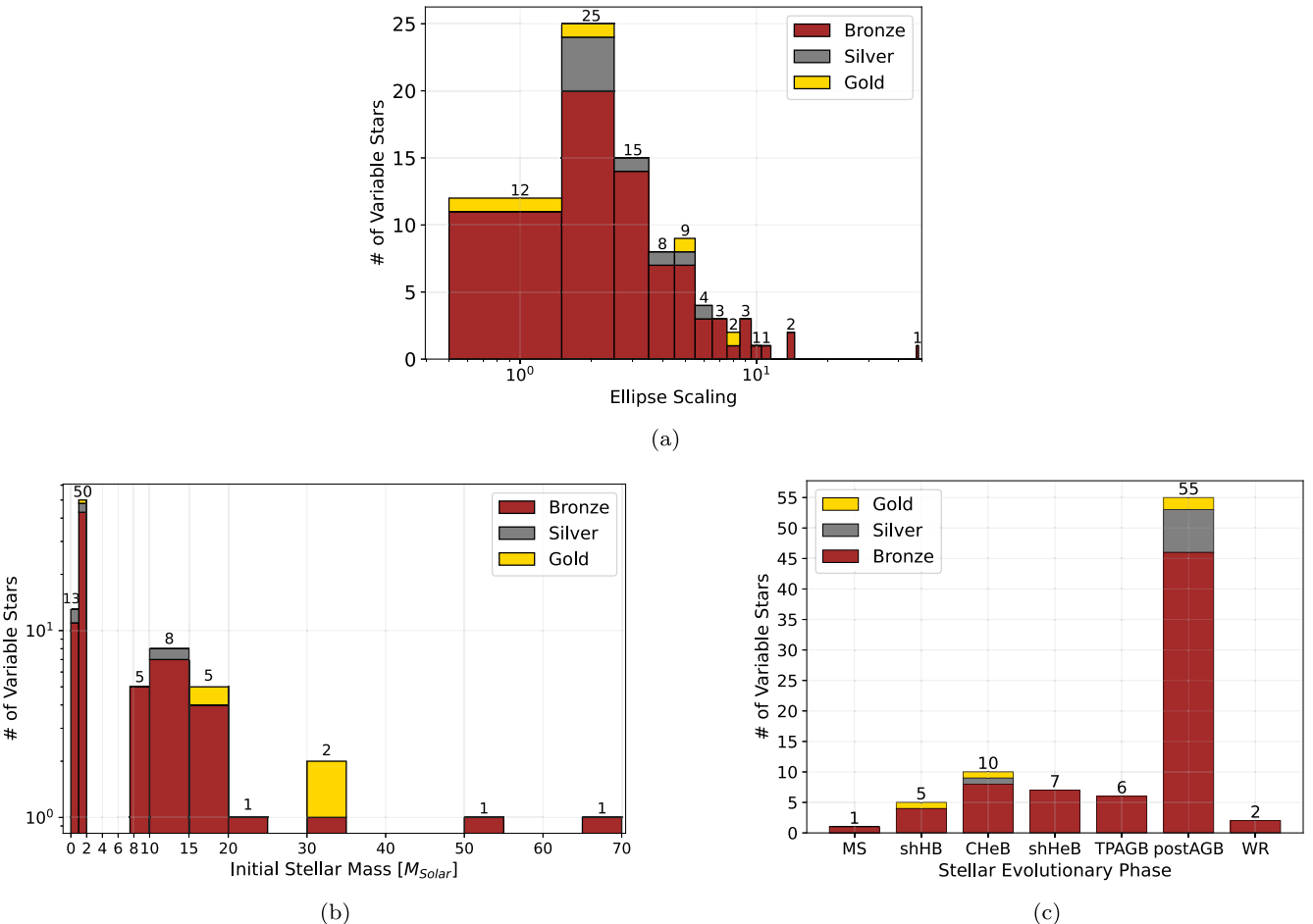


Figure 12. Distributions of stellar parameters derived from the isochrone analysis described in Section 4.1: (a) error-ellipse scaling factor; (b) stellar initial mass, M_{init} ; (c) stellar evolutionary phase. The *Gold*, *Silver*, and *Bronze* classification of each cluster-variable star is defined in Section 4.3.

the difference between the measured host cluster age, metallicity and extinction values obtained by Caldwell et al. and de Meulenaer et al. as the uncertainty estimates on these properties, along with the A. W. McConnachie et al. (2005) distance modulus (24.47 ± 0.07). We repeat the MIST isochrone generation and matching process described above for every combination of discrete upper-, middle-, and lower-limit values of the cluster 3801 age ($\log(\text{Age}) \in 9.8, 11.7, 13.6$), metallicity ($Z \in -0.1, 0.1, 0.3$), extinction ($E(B-V) \in 0.07, 0.24, 0.41$), and distance modulus ($(m-M) \in 24.40, 24.47, 24.54$), examining the isochrone matches produced for its confirmed cluster-variable star.

The resulting isochrone matches show no change in evolutionary phase with changing host cluster properties compared to those obtained using de Meulenaer et al. values. The remaining isochrone-derived stellar properties show the greatest change as a result of varying cluster age. Matches to the youngest cluster isochrones ($\log(\text{Age}) = 9.8$) return more luminous stars ($F814W \sim -5.0$) with a broader range of stellar colors ($1.1 \leq F475W - F814W \leq 1.7$) and higher initial stellar masses ($1.1 M_{\odot} < M_{\text{init}} < 1.3 M_{\odot}$). Matches to older cluster isochrones ($\log(\text{Age}) \in 11.7, 13.6$) produce fainter stars ($-4.6 \leq F814W \leq -4.4$) with bluer colors ($0.9 \leq F475W - F814W \leq 1.4$) and smaller initial stellar masses ($0.8 M_{\odot} < M_{\text{init}} < 1 M_{\odot}$). We find that the youngest isochrones ($\log(\text{Age}) = 9.8$) produce matches with increasingly

blue stellar colors as host cluster metallicity increases, while older cluster isochrones return increasingly red stellar colors. Increasing host cluster metallicity increases both the initial mass and luminosity of the variable star for host cluster isochrones of all ages. We find no change in isochrone-derived stellar parameters attributable to varying extinction or distance modulus. Based on this representative host cluster example and using informal uncertainties on host cluster properties, we determine that uncertainties in host cluster age and, to a lesser extent, metallicity dominate the isochrone matching process implemented in this study; see, however, the caveats in Section 4.5.

Figure 12 shows the distribution of error-ellipse scale factors for the 86 confirmed variable stars, as well as the resulting distributions of initial stellar mass and evolutionary phase obtained from the isochrone analysis above. In terms of error-ellipse scaling factors, 37 of the 86 variable stars (43%) require scaling factors of <3 , increasing to 60 (70%) requiring scaling factors of <5 . Broken down by phase, we find that the 86 cluster-variable stars in our sample comprise one MS, 5 hydrogen-shell burning (shHB), 10 core-helium burning (CHeB), 7 helium-shell-burning (shHeB), 6 TPAGB, 55 post-AGB, and 2 Wolf-Rayet (W-R) stars. The initial masses of the stars in our sample range between 0.8 and $67 M_{\odot}$. We caution that these results remain subject to the effects of blending, as described in Section 4.3, as well as additional caveats detailed in Section 4.5.

Table 3
Properties of Each of the 89 Cluster-variable Stars Confirmed through DI Pipeline Analysis

PHAT ID	Variable Star Properties								Host Cluster Properties						
	F814W (mag)		F475W – F814W		Stellar	Blending	Ranking	M_{init} (M_{\odot})	Phase	Cluster ID	R.A. (deg)	Decl. (deg)	Age (Log(yr))	A_v (mag)	Z
	Obs.	Iso.	Obs.	Iso.											
PHAT_11.1262019 +41.843634	-5.616	-5.278	4.339	1.678	Ambiguous	Least	Bronze	1.57	Post-AGB	230	11.127033	41.843671	9.30	0.06	-0.40
PHAT_10.9115373 +41.380738	-6.587	-6.411	3.285	3.864	Ambiguous	Least	Bronze	7.77	TPAGB	390	10.911579	41.380726	7.65	0.12	0.02
PHAT_11.1047292 +41.346899	-7.422	-7.879	0.967	-0.214	Good	Least	Gold	33.23	shHB	403	11.104662	41.347108	6.75	0.45	0.02
PHAT_11.1050349 +41.347152	-6.106	-6.558	0.555	-0.378	Ambiguous	Likely	Bronze	33.20	MS	403	11.104662	41.347108	6.75	0.45	0.02
PHAT_10.9517333 +41.448087	-6.820	-5.055	1.798	3.041	Ambiguous	Highly	Bronze	1.08	TPAGB	445	10.951771	41.448099	9.65	0.22	-1.80
PHAT_10.9517775 +41.448073	-6.366	-5.055	1.732	3.041	Ambiguous	Highly	Bronze	1.08	TPAGB	445	10.951771	41.448099	9.65	0.22	-1.80
PHAT_10.9517795 +41.448104	-6.000	-5.055	1.454	3.041	Ambiguous	Likely	Bronze	1.08	TPAGB	445	10.951771	41.448099	9.65	0.22	-1.80
PHAT_11.1676358 +41.250191	-5.897	-3.798	1.464	1.961	Ambiguous	Highly	Bronze	0.99	CHeB	483	11.167649	41.250178	9.80	0.18	-2.20
PHAT_11.1676294 +41.250149	-6.507	-3.798	1.531	1.961	Ambiguous	Likely	Bronze	0.99	CHeB	483	11.167649	41.250178	9.80	0.18	-2.20
PHAT_11.1676700 +41.250131	-5.686	-3.798	1.415	1.961	Ambiguous	Highly	Bronze	0.99	CHeB	483	11.167649	41.250178	9.80	0.18	-2.20
PHAT_11.6125244 +42.031279	-5.865	-4.958	1.608	1.694	Ambiguous	Highly	Bronze	1.14	Post-AGB	540	11.612541	42.031319	9.65	0.12	-0.80
PHAT_11.6125277 +42.031316	-6.359	-4.958	1.706	1.694	Ambiguous	Highly	Bronze	1.14	Post-AGB	540	11.612541	42.031319	9.65	0.12	-0.80
PHAT_11.1383029 +41.886371	-6.211	-6.368	1.026	1.290	Ambiguous	Highly	Bronze	9.15	CHeB	609	11.138301	41.886391	7.50	0.56	0.02
PHAT_11.1381453 +41.886387	-7.120	-6.673	2.228	3.836	Ambiguous	Least	Bronze	9.19	shHeB	609	11.138301	41.886391	7.50	0.56	0.02
PHAT_10.9923715 +41.410639	-5.779	-4.958	1.744	1.694	Good	Likely	Silver	1.14	Post-AGB	626	10.992397	41.410646	9.65	0.12	-0.80
PHAT_10.7148817 +41.391778	-6.826	-7.067	3.274	0.067	Good	Least	Gold	15.14	CHeB	662	10.715145	41.391583	7.10	0.20	0.02
PHAT_10.7152697 +41.391582	-6.859	-7.813	82.188	4.031	Ambiguous	Least	Bronze	16.35	shHeB	662	10.715145	41.391583	7.10	0.20	0.02
PHAT_10.9139786 +41.168986	-7.127	-7.498	0.450	1.038	Ambiguous	Least	Bronze	13.49	CHeB	693	10.914089	41.169140	7.20	0.33	0.02
PHAT_11.4280933 +41.756429	-6.588	-7.270	0.761	-0.054	Ambiguous	Least	Bronze	18.17	shHB	711	11.427535	41.756568	7.00	0.68	0.02
PHAT_10.9665814 +41.263916	-6.148	-5.976	0.564	1.327	Ambiguous	Least	Bronze	8.19	CHeB	742	10.966655	41.264048	7.60	0.53	0.02
PHAT_11.1754618 +41.731831	-5.704	-5.025	1.671	3.861	Good	Highly	Bronze	1.04	TPAGB	757	11.175425	41.731819	9.75	0.11	-1.00
PHAT_11.1932671 +41.488258	-6.142	-4.743	1.581	1.678	Ambiguous	Highly	Bronze	1.02	Post-AGB	859	11.193255	41.488278	9.90	0.06	-0.40

Table 3
(Continued)

PHAT ID	Variable Star Properties								Host Cluster Properties							
	F814W (mag)		F475W – F814W		Stellar	Blending	Ranking	M_{init} (M_{\odot})	Phase	Cluster ID	R.A. (deg)	Decl. (deg)	Age (Log(yr))	A_v (mag)	Z	
	Obs.	Iso.	Obs.	Iso.												
14	PHAT_11.2445990 +41.910174	-6.492	-6.901	1.645	3.217	Ambiguous	Likely	Bronze	11.85	shHeB	980	11.244653	41.910184	7.30	0.57	0.02
	PHAT_11.2446190 +41.910229	-6.533	-6.326	1.055	0.768	Ambiguous	Likely	Bronze	11.20	shHB	980	11.244653	41.910184	7.30	0.57	0.02
	PHAT_11.2445324 +41.910222	-6.196	-6.713	2.356	2.959	Good	Likely	Silver	11.84	CHeB	980	11.244653	41.910184	7.30	0.57	0.02
	PHAT_11.1798774 +41.868042	-7.034	-7.179	3.081	4.074	Ambiguous	Least	Bronze	11.86	shHeB	1026	11.179935	41.868007	7.30	0.25	0.02
	PHAT_10.8783069 +41.354624	-5.735	-5.263	1.762	1.569	Ambiguous	Highly	Bronze	1.01	Post-AGB	1052	10.878286	41.354559	9.75	0.15	-1.80
	PHAT_10.8783503 +41.354581	-5.924	-5.263	1.907	1.569	Ambiguous	Highly	Bronze	1.01	Post-AGB	1052	10.878286	41.354559	9.75	0.15	-1.80
	PHAT_10.9942367 +41.505036	-5.937	-5.070	1.697	1.626	Ambiguous	Highly	Bronze	1.16	Post-AGB	1137	10.994251	41.505051	9.60	0.14	-1.00
	PHAT_10.9942370 +41.505079	-5.837	-5.070	1.810	1.626	Ambiguous	Highly	Bronze	1.16	Post-AGB	1137	10.994251	41.505051	9.60	0.14	-1.00
	PHAT_11.1970592 +41.473290	-5.925	-6.358	0.528	-0.500	Ambiguous	Least	Bronze	51.83	W-R	1230	11.197085	41.473312	6.65	0.38	0.02
	PHAT_10.7799717 +41.196765	-5.637	-4.836	2.098	1.664	Ambiguous	Likely	Bronze	1.03	Post-AGB	1309	10.779986	41.196790	9.95	0.14	-0.20
	PHAT_10.8142021 +41.190278	-5.758	-5.074	1.623	1.721	Good	Highly	Bronze	1.16	Post-AGB	1416	10.814255	41.190281	9.60	0.13	-1.00
	PHAT_10.8142534 +41.190277	-6.687	-5.074	1.553	1.721	Good	Least	Gold	1.16	Post-AGB	1416	10.814255	41.190281	9.60	0.13	-1.00
	PHAT_11.4220892 +41.739675	-7.219	-7.658	3.353	4.095	Ambiguous	Least	Bronze	15.00	shHeB	1423	11.422059	41.739605	7.15	0.48	0.02
	PHAT_10.7151784 +41.234343	-5.637	-4.668	1.734	1.673	Good	Highly	Bronze	0.90	Post-AGB	1642	10.715190	41.234370	10.00	0.08	-0.80
	PHAT_11.0146309 +41.510745	-6.213	-4.612	1.469	1.334	Good	Highly	Bronze	0.86	Post-AGB	1680	11.014600	41.510742	10.10	0.08	-0.60
	PHAT_10.7899451 +41.359062	-5.983	-4.635	2.394	1.652	Good	Likely	Silver	0.86	Post-AGB	1797	10.789821	41.358924	10.10	0.31	-0.60
	PHAT_10.7898296 +41.358822	-5.911	-4.635	2.450	1.652	Good	Highly	Bronze	0.86	Post-AGB	1797	10.789821	41.358924	10.10	0.31	-0.60
	PHAT_10.7897138 +41.358912	-5.856	-4.635	2.187	1.652	Good	Highly	Bronze	0.86	Post-AGB	1797	10.789821	41.358924	10.10	0.31	-0.60
	PHAT_10.7896724 +41.358971	-5.865	-4.635	2.363	1.652	Good	Likely	Silver	0.86	Post-AGB	1797	10.789821	41.358924	10.10	0.31	-0.60
	PHAT_10.8795858 +41.304103	-5.832	-4.763	1.645	1.534	Ambiguous	Highly	Bronze	0.99	Post-AGB	1802	10.879593	41.304081	9.85	0.09	-0.80
	PHAT_10.8796413 +41.304089	-6.007	-4.763	1.495	1.534	Ambiguous	Highly	Bronze	0.99	Post-AGB	1802	10.879593	41.304081	9.85	0.09	-0.80
	PHAT_11.1813291 +41.443916	-6.845	-7.067	0.051	0.067	Ambiguous	Least	Bronze	15.14	CHeB	1825	11.181320	41.443749	7.10	0.21	0.02

Table 3
(Continued)

PHAT ID	Variable Star Properties								Host Cluster Properties						
	F814W (mag)		F475W – F814W		Stellar	Blending	Ranking	M_{init} (M_{\odot})	Phase	Cluster ID	R.A. (deg)	Decl. (deg)	Age (Log(yr))	A_v (mag)	Z
	Obs.	Iso.	Obs.	Iso.											
PHAT_11.4242884 +41.759313	-5.884	-4.836	1.878	1.664	Ambiguous	Likely	Bronze	1.03	Post-AGB	1920	11.424344	41.759294	9.95	0.07	-0.20
PHAT_11.4242968 +41.759278	-6.389	-4.836	1.983	1.664	Ambiguous	Highly	Bronze	1.03	Post-AGB	1920	11.424344	41.759294	9.95	0.07	-0.20
PHAT_11.4243211 +41.759318	-6.103	-4.836	1.821	1.664	Good	Likely	Silver	1.03	Post-AGB	1920	11.424344	41.759294	9.95	0.07	-0.20
PHAT_11.4243543 +41.759330	-6.063	-4.836	1.884	1.664	Good	Highly	Bronze	1.03	Post-AGB	1920	11.424344	41.759294	9.95	0.07	-0.20
PHAT_10.8380804 +41.235576	-5.641	-4.683	2.767	1.660	Ambiguous	Likely	Bronze	0.89	Post-AGB	2012	10.838010	41.235617	10.10	0.08	-0.40
PHAT_10.8582937 +41.358786	-5.541	-4.710	1.740	1.710	Ambiguous	Highly	Bronze	0.95	Post-AGB	2125	10.858304	41.358815	10.00	0.06	-0.40
PHAT_11.0284722 +41.674479	-5.555	-5.661	-0.136	-0.378	Ambiguous	Least	Bronze	22.40	shHB	2143	11.028640	41.674386	6.90	0.07	0.02
PHAT_11.2413408 +41.489948	-5.619	-5.148	1.641	1.175	Good	Highly	Bronze	1.30	Post-AGB	2348	11.241335	41.489975	9.55	0.07	-0.40
PHAT_10.8938331 +41.161436	-5.923	-6.264	0.221	-0.505	Ambiguous	Least	Bronze	66.15	W-R	2672	10.893817	41.161411	6.60	0.36	0.02
PHAT_10.7833409 +41.305080	-5.753	-4.890	1.949	1.731	Good	Highly	Bronze	1.33	Post-AGB	2683	10.783367	41.305101	9.70	0.09	0.20
PHAT_11.1534065 +41.876700	-6.605	-6.909	3.882	3.238	Ambiguous	Likely	Bronze	11.85	shHeB	2805	11.153462	41.876728	7.30	0.30	0.02
PHAT_10.9480593 +41.452227	-6.173	-4.907	2.097	0.968	Ambiguous	Highly	Bronze	1.17	Post-AGB	3088	10.948064	41.452235	9.70	0.09	-0.40
PHAT_10.7637717 +41.356039	-7.180	-4.878	1.929	1.705	Good	Highly	Bronze	1.04	Post-AGB	3510	10.763763	41.356043	10.00	0.06	0.00
PHAT_10.7637208 +41.356041	-6.125	-4.879	1.658	1.613	Good	Highly	Bronze	1.04	Post-AGB	3510	10.763763	41.356043	10.00	0.06	0.00
PHAT_10.6854970 +41.244921	-5.909	-5.001	2.039	1.686	Good	Highly	Bronze	1.17	Post-AGB	3704	10.685397	41.244901	9.65	0.20	-0.60
PHAT_10.6853726 +41.244896	-6.304	-5.001	1.815	1.686	Good	Highly	Bronze	1.17	Post-AGB	3704	10.685397	41.244901	9.65	0.20	-0.60
PHAT_10.6854787 +41.244965	-6.148	-5.001	2.231	1.686	Ambiguous	Likely	Bronze	1.17	Post-AGB	3704	10.685397	41.244901	9.65	0.20	-0.60
PHAT_10.6854764 +41.244798	-6.378	-5.001	2.027	1.686	Good	Likely	Silver	1.17	Post-AGB	3704	10.685397	41.244901	9.65	0.20	-0.60
PHAT_10.6854201 +41.244921	-6.500	-5.001	1.952	1.686	Ambiguous	Highly	Bronze	1.17	Post-AGB	3704	10.685397	41.244901	9.65	0.20	-0.60
PHAT_10.6854053 +41.244830	-6.364	-4.998	1.741	1.600	Ambiguous	Highly	Bronze	1.17	Post-AGB	3704	10.685397	41.244901	9.65	0.20	-0.60
PHAT_10.6854095 +41.244870	-6.450	-5.001	1.656	1.686	Good	Highly	Bronze	1.17	Post-AGB	3704	10.685397	41.244901	9.65	0.20	-0.60
PHAT_10.6853291 +41.244909	-5.719	-4.998	1.716	1.600	Good	Likely	Silver	1.17	Post-AGB	3704	10.685397	41.244901	9.65	0.20	-0.60

Table 3
(Continued)

PHAT ID	Variable Star Properties								Host Cluster Properties						
	F814W (mag)		F475W – F814W		Stellar	Blending	Ranking	M_{init} (M_{\odot})	Phase	Cluster ID	R.A. (deg)	Decl. (deg)	Age (Log(yr))	A_v (mag)	Z
	Obs.	Iso.	Obs.	Iso.											
PHAT_10.6855112 +41.244854	-6.368	-5.001	1.989	1.686	Ambiguous	Likely	Bronze	1.17	Post-AGB	3704	10.685397	41.244901	9.65	0.20	-0.60
PHAT_10.6853552 +41.244936	-5.785	-4.998	1.846	1.600	Good	Highly	Bronze	1.17	Post-AGB	3704	10.685397	41.244901	9.65	0.20	-0.60
PHAT_10.6853832 +41.244965	-5.876	-5.001	2.052	1.686	Good	Highly	Bronze	1.17	Post-AGB	3704	10.685397	41.244901	9.65	0.20	-0.60
PHAT_10.6853209 +41.244828	-6.286	-4.998	1.806	1.600	Good	Highly	Bronze	1.17	Post-AGB	3704	10.685397	41.244901	9.65	0.20	-0.60
PHAT_10.6852844 +41.244888	-5.723	-5.001	1.826	1.686	Good	Highly	Bronze	1.17	Post-AGB	3704	10.685397	41.244901	9.65	0.20	-0.60
PHAT_10.6853654 +41.244792	-5.932	-5.001	1.794	1.686	Ambiguous	Highly	Bronze	1.17	Post-AGB	3704	10.685397	41.244901	9.65	0.20	-0.60
PHAT_10.6853373 +41.244875	-6.141	-5.001	1.823	1.686	Good	Highly	Bronze	1.17	Post-AGB	3704	10.685397	41.244901	9.65	0.20	-0.60
PHAT_10.6853590 +41.244846	-6.093	-5.001	1.830	1.686	Good	Likely	Silver	1.17	Post-AGB	3704	10.685397	41.244901	9.65	0.20	-0.60
PHAT_10.7494354 +41.268271	-7.016	-4.999	1.914	1.648	Good	Least	Gold	1.19	Post-AGB	3801	10.749432	41.268276	9.80	0.07	0.00
PHAT_11.1832836 +41.440709	-5.724	-5.802	1.503	1.573	Ambiguous	Least	Bronze	9.81	shHB	3909	11.182722	41.439833	7.40	0.07	0.02
PHAT_10.7485055 +41.322014	-6.496	-4.896	1.918	1.660	Good	Highly	Bronze	1.07	Post-AGB	3983	10.748530	41.322039	9.95	0.08	0.00
PHAT_10.7485231 +41.322048	-6.628	-4.896	1.860	1.660	Good	Highly	Bronze	1.07	Post-AGB	3983	10.748530	41.322039	9.95	0.08	0.00
PHAT_11.1712113 +41.875049	-7.620	-7.179	3.784	4.074	Ambiguous	Least	Bronze	11.86	shHeB	4434	11.171222	41.875064	7.30	0.13	0.02
PHAT_11.1838224 +41.443995	-6.805	-6.948	0.149	-0.001	Ambiguous	Least	Bronze	15.14	CHeB	4775	11.182554	41.443443	7.10	0.17	0.02
PHAT_10.6385785 +41.295080	-5.875	-4.912	2.070	1.571	Ambiguous	Highly	Bronze	1.09	Post-AGB	5002	10.638539	41.295119	10.00	0.08	0.20
PHAT_10.6385439 +41.295103	-6.625	-4.907	2.152	1.740	Good	Highly	Bronze	1.09	Post-AGB	5002	10.638539	41.295119	10.00	0.08	0.20
PHAT_10.7550717 +41.269539	-5.691	-5.484	2.009	1.634	Good	Highly	Bronze	1.29	Post-AGB	5105	10.755098	41.269581	9.75	0.09	0.20
PHAT_10.7550909 +41.269571	-6.522	-5.491	1.976	1.316	Good	Highly	Bronze	1.29	Post-AGB	5105	10.755098	41.269581	9.75	0.09	0.20
PHAT_10.6480674 +41.242849	-6.339	-5.409	1.531	3.499	Ambiguous	Highly	Bronze	1.25	TPAGB	5117	10.647973	41.242830	9.45	0.25	-1.80
PHAT_10.6920206 +41.293412	-5.895	-4.896	1.977	1.660	Good	Highly	Bronze	1.07	Post-AGB	8052	10.692013	41.293419	9.95	0.07	0.00

Note. Host cluster properties obtained from P. de Meulenaer et al. (2017). Star IDs (PHAT ID) are those used in the PHAT survey and include the catalog-recorded R.A. and decl. of the star in decimal degrees. Variable star F814W magnitudes and F475W – F814W colors are divided into observed (Obs.) and isochrone-derived values (Iso.; see Section 4.2), the latter used in Figures 15 and 16.

Table 3 contains the results of all 86 variable stars, including observed and isochrone-derived F475W – F814W color and F814W absolute magnitudes, stellar evolutionary phase, and initial mass, in addition to the age, extinction, and metallicity properties of their host clusters obtained from P. de Meulenaer et al. (2017) used in isochrone generation.

4.3. Prevalence of Blending

Since we derive the properties of the cluster-variable stars using their PHAT photometry in the previous section, we must consider the effects of light blending in their photometry. The effect of this blending is to boost the measured magnitude of a source, which can produce a near-vertical “plume” of stars on the host cluster CMD in cases of extreme blending. Fully accounting for this blending is difficult and beyond the scope of this work. Instead, we assess the probability of each cluster-variable star being dominated by blending based on the measured properties of blended and unblended stars in the PHAT clusters. We identify two parameters to help describe the potential level of blending for each cluster star in the PHAT survey: the F814W crowding value produced by DOLPHOT (A. E. Dolphin 2000) during PHAT survey source detection (described in J. J. Dalcanton et al. 2012; B. F. Williams & J. J. Dalcanton et al. 2014) and the distance D_{cluster} between the star and its host cluster center.

We then characterize the crowding and D_{cluster} behavior at varying degrees of blending by selecting representative samples of likely and less likely to be blended cluster stars from the PHAT survey. We select our blended star sample by first identifying globular clusters in the PHAT survey with age estimates >10 Gyr, their greater stellar densities making blending effects in the photometry of detected constituent stars more likely. We produce a CMD for each globular cluster with age >10 Gyr along with its isochrone, generated as described in Section 4.1, which we use to identify the “plume” of blended stars in the cluster, if present. We select such stars from those clusters with an unambiguous plume above its isochrone as our blended sample. For our unblended star sample, we consider younger (ages <1 Gyr), and therefore lower stellar density, PHAT survey clusters. From these young clusters, we select stars that are in good agreement with their host cluster isochrone to use as our unblended sample. Example cluster CMDs showing the regions used to select blended and unblended stars are shown in Figure 13. Our final samples comprise 141 blended stars from five old globular clusters and 101 unblended stars from seven young clusters.

We obtain the crowding and D_{cluster} parameters for both sets of sampled stars, which are plotted in Figure 13. A clear correlation between decreasing D_{cluster} and increasing crowding can be seen for the blended stars. We then perform kernel density estimations (KDEs) for the blended and unblended groups using the Gaussian_kde package from the scipy.stats library. The resulting KDEs are also shown in Figure 13. The blended KDE (red contours) exhibits the greatest density between $0.^{\circ}2 < D_{\text{cluster}} < 1^{\circ}$ and $0.15 \text{ mag} < \text{crowding} < 1 \text{ mag}$. The unblended KDE (blue contours) extends to larger D_{cluster} values, with the highest densities occurring for crowding $\lesssim 0.15 \text{ mag}$, though with a clear overlap between blended and unblended KDEs.

We now use the blended and unblended KDEs to calculate the a posteriori blending probability for each of the 86 cluster-

variable stars in our sample, following

$$P(B|(x, y)) = \frac{P((x, y)|B)}{P((x, y)|B) + P((x, y)|U)}, \quad (3)$$

where x and y are the D_{cluster} and crowding values of the cluster-variable star, respectively; $P((x, y)|B)$ is the likelihood of the star being blended, obtained by evaluating the blended KDE at (x, y) ; and $P((x, y)|U)$ is the likelihood of the star being unblended, obtained by evaluating the unblended KDE at (x, y) .

We examine the resulting distribution of a posteriori blending probabilities for the 86 cluster-variable stars shown in Figure 14 to determine the thresholds by which we describe our level of confidence in the measured PHAT photometry being dominated by a single source based on measured PHAT source behaviors. Based on this distribution, we determine

1. $P(B|(x, y)) < 0.32$: star is *least likely blended*;
2. $0.32 \leq P(B|(x, y)) < 0.8$: star is *likely blended*; and
3. $P(B|(x, y)) \geq 0.8$: star is *highly likely blended*.

Of the 86 cluster-variable stars, we find 20 to be *least likely blended*, 19 *likely blended*, and 47 *highly likely blended*.

We now incorporate the blending probability category for each of our cluster-variable stars into a final classification, combining blending probability and our difference image source detection analysis described in Section 3.4.3, as follows.

1. *Gold*: *Good* detection and *least likely blended*.
2. *Silver*: *Good* detection and *likely blended*.
3. *Bronze*: *Ambiguous* detection and *highly likely blended*.

Our sample of 86 cluster-variable stars therefore comprises 4 *Gold*, 8 *Silver*, and 74 *Bronze* quality results. These final classifications are shown in the ellipse scaling, initial stellar mass, and stellar phase distributions in Figure 12. Based on the *Good* difference image source detections and lower probability of blended photometry, we assign a higher level of confidence to the 12 *Gold*- and *Silver*-class stars in our sample.

As previously noted, the observed PHAT photometry of our cluster-variable stars is unlikely to represent their equilibrium states due to the sparsely sampled PHAT measurements. We therefore produce CMDs of our cluster-variable stars using the theoretical color and magnitude values of the most probable datum on their host cluster isochrone, constituting their most likely equilibrium state based on the available PHAT data. Figure 15 shows the theoretical isochrone F475W – F814W color versus F814W absolute magnitude CMD for these 12 *Gold* and *Silver* cluster-variable stars using the color and magnitude values from the most probable datum on their host cluster isochrone; the figure also includes their initial masses and evolutionary phases. Similarly, Figure 16 shows the theoretical isochrone F475W – F814W color versus F814W absolute magnitude CMD for all 86 cluster-variable stars in our sample. We refer to the positions of each cluster-variable star on these CMDs, in addition to their light-curve properties, initial mass, and evolutionary phase, when determining the type of variability shown by each star in the following section.

4.4. Variable Star Classification

We are able to assign variable star classifications to the 86 confirmed cluster-variable stars in our sample using the combined information of their light-curve amplitudes, colors,

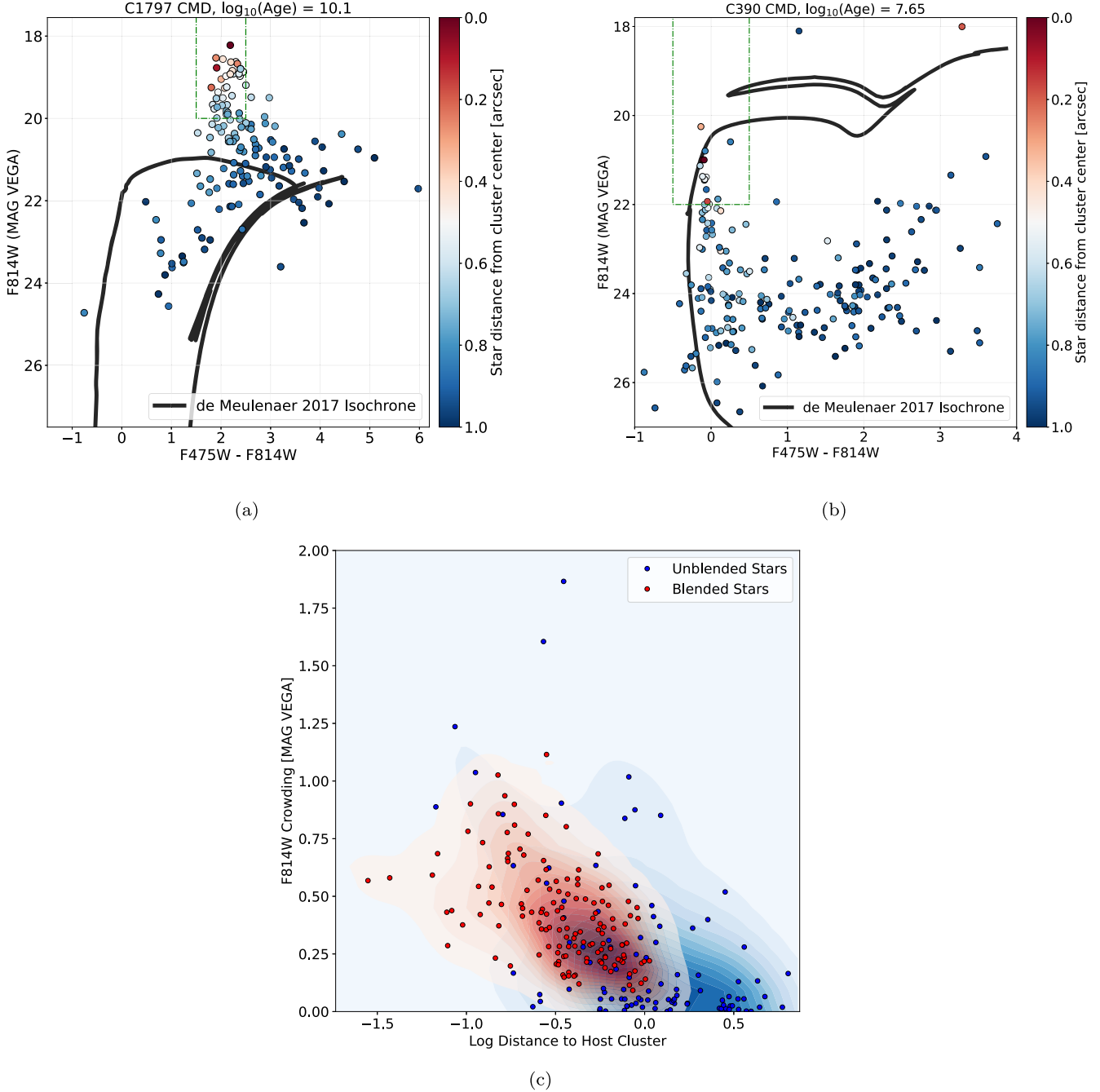


Figure 13. CMDs of clusters 1797 (a) and 390 (b) (Johnson et al. cluster IDs), demonstrating the selection of blended (“plume”) and unblended stars described in Section 4.3 (areas enclosed by green dotted-dashed lines). The D_{cluster} vs. F814W crowding parameter values for the blended and unblended cluster stars is shown in (c), along with their KDEs (red and blue contours, respectively). These KDEs are sampled to calculate the likelihood of each cluster-variable star being blended, following Equation (3).

brightness values, and, for the first time, evolutionary phases and initial masses.

Beginning with the most numerous stars in our sample, the 55 variable stars in the post-AGB phase make up the majority of our cluster-variable star sample, with initial masses in the range $0.8\text{--}1.6 M_{\odot}$ and median initial mass $\sim 1.1 M_{\odot}$. The most likely current stellar masses for the 55 RV Tauri stars in our sample ($0.53 M_{\odot} \leq M_{\text{current}} < 0.59 M_{\odot}$) are consistent with those typical of post-AGB stars ($0.55\text{--}1.1 M_{\odot}$; M. A. T. Groenewegen & M. I. Jurkovic 2017). Based on their initial mass range and late evolutionary phase, we tentatively classify all 55 post-AGB stars as RV Tauri-type variables. Despite occupying

approximately the same region of the CMD as classical Cepheids, as shown in Figures 15 and 16, RV Tauri stars are the luminous, long-period extension of Type II Cepheids (M. Jura 1986; C. Alcock et al. 1998; L. L. Kiss et al. 2007; A. Bódi & L. L. Kiss 2019). They have periods of $\sim 20\text{--}150$ days and a characteristic light curve exhibiting alternating deeper and shallower minima (G. Wallerstein 2002; L. L. Kiss et al. 2007; M. I. Jurkovic 2021), potentially indicating a double-mode pulsation mechanism (M. Takeuti & J. O. Petersen 1983) or chaotic behavior (J. R. Buchler & G. Kovacs 1987). Infrared excesses in RV Tauri observations have been attributed to circumstellar dust,

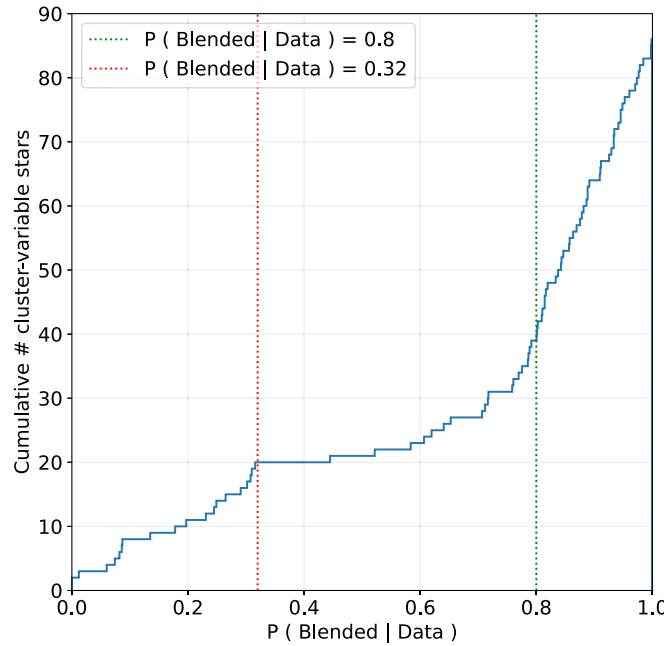


Figure 14. Cumulative distribution of blending probabilities for the 86 cluster-variable stars in our sample. The red and green vertical dotted lines denote the adopted threshold probability values between the *likely/highly likely blended* and *least likely/likely blended* categories, respectively, as described in Section 4.3.

the presence and nature of which can inform the singular/binary origin of the star. More luminous RV Tauri stars with disk-type excesses and initial stellar mass $>1 M_{\odot}$ are likely the product of binary interactions (R. Manick et al. 2018), while less luminous, dusty RV Tauri stars are likely post-RGB binaries with lower current masses identified by D. Kamath et al. (2016). RV Tauri stars with no infrared excess may be either a single post-AGB with initial stellar mass $\lesssim 1.25 M_{\odot}$, with any circumstellar dust having dissipated ~ 1000 yr after the onset of its post-AGB phase (R. Manick et al. 2018), or a binary post-RGB with initial stellar mass $<1 M_{\odot}$ in which the star evolves sufficiently slowly for the dust to have dissipated. Spectral energy distributions of the RV Tauri stars in our sample are required to identify any infrared excess and diagnose their potential origins. Alternatively, some of these post-AGB stars could be Yellow Semiregular variables (SRDs). SRDs are closely related to RV Tauri stars, occupying the same magnitude and color space and sharing similar initial masses; however, any deep–shallow alternating light-curve pattern is indistinguishable (J. R. Percy 2022). The light curve for one of the post-AGB stars in our sample is shown in Figure 17, demonstrating that the sparsely sampled PHAT survey data alone are insufficient to allow identification of RV Tauri behavior for the stars in our sample. That said, the distinctive RV Tauri light-curve behavior would potentially allow for easy verification for these stars using longer-baseline follow-up observations designed around the ~ 20 –150 day pulsation periods of these targets.

While post-AGB stars comprise the majority of stars in our sample despite their rarity caused by the short-lived nature of this evolutionary phase, we note that 46 of our post-AGB stars are classified as *Bronze*, of which 40 are *highly likely* and five *likely* affected by blending, and seven are classified as *Silver*, all of which are *likely* affected by blending. We therefore attribute lower confidence to these 53 *Bronze* and *Silver* post-

AGBs than the remaining two *Gold, least likely blended* post-AGB stars in our sample, shown with black-edged markers in Figure 15.

The single red ($F475W - F814W \sim 3$) CHeB star with $F814W \sim -6.7$ mag in Figures 15 and 16 is a *Silver-class* result, with an initial stellar mass of $11.8 M_{\odot}$. The red color and increased luminosity of this CHeB star are consistent with the properties of red supergiant (RSG) stars. RSGs are the direct progenitors to Type II-P supernovae, with initial stellar masses ranging from $9 M_{\odot}$ to ~ 30 – $40 M_{\odot}$ (G. Meynet & A. Maeder 2000; R. M. Humphreys et al. 2020) and semiregular variability over long periods of up to a few thousand days, potentially making characterizing their variability a challenge (A. Heger et al. 1997; M. D. Soraisam et al. 2018). The variability of RSGs is thought to be driven by the interaction of atmospheric convection and the κ -mechanism in a zone of hydrogen ionization within their atmospheres. The κ -mechanism is a cyclical process of pulsations within a stellar atmosphere in which a layer of material increases in opacity as its temperature and density increase (such as the hydrogen ionization layer moving radially inward in an RSG star), resulting in an increase in radiation pressure on the layer from the stellar core that pushes the layer back out.

The seven *Bronze* shHeB variable stars in our sample are also luminous ($F814W < -6.5$ mag) and show red colors ($F475W - F814W > 3$). The initial stellar masses of these stars range between 9 and $17 M_{\odot}$, which is again consistent with the known properties of RSG variable stars outlined above (A. Heger et al. 1997; M. D. Soraisam et al. 2018; R. M. Humphreys et al. 2020). We therefore also designate these seven evolved, red, shHeB stars as RSG variables. An example light curve for one of the shHeB RSG stars in our sample is included in Figure 17.

A previous study by L. C. Johnson et al. (2012) identified about 15 candidate RSG clusters (i.e., clusters hosting RSGs) using data available from the first year of the PHAT survey. To check whether the eight RSGs from this work correspond to those in this previous study, we cross-match the host clusters of our RSGs with those from L. C. Johnson et al. (2012) using a radius of $1''$, finding five matches. We thus confirm five of the Johnson et al. RSG candidates via variability analysis and find three new RSGs in PHAT survey clusters.

The *Bronze-class* luminous ($F814W \sim -6.4$), red ($F475W - F814W \sim 3.9$) TPAGB star is distinct from the other TPAGB cluster variables in our sample and appears consistent with the properties of the RSGs outlined above, as shown in Figure 16. Its late evolutionary stage, increased luminosity, and high initial mass of $\sim 8 M_{\odot}$ are consistent with this star being a super-AGB (SAGB) variable candidate. SAGBs span the low-to-high stellar mass range (~ 6 – $12 M_{\odot}$), with higher-mass SAGBs being potential supernova progenitors while lower-mass SAGBs evolve to white dwarf stars (C. L. Doherty et al. 2017; Daichi Hiramatsu et al. 2021). SAGBs occupy similar color and magnitude space as RSGs, making them nearly indistinguishable bar the potential exception of RSGs having lower variability (C. L. Doherty et al. 2017). While we classify this SAGB candidate as a *Bronze* result, our blending analysis shows it as *least likely* to be affected by blending, making it an intriguing candidate SAGB star for follow-up observation and verification through measurement of its thermal pulsation period.

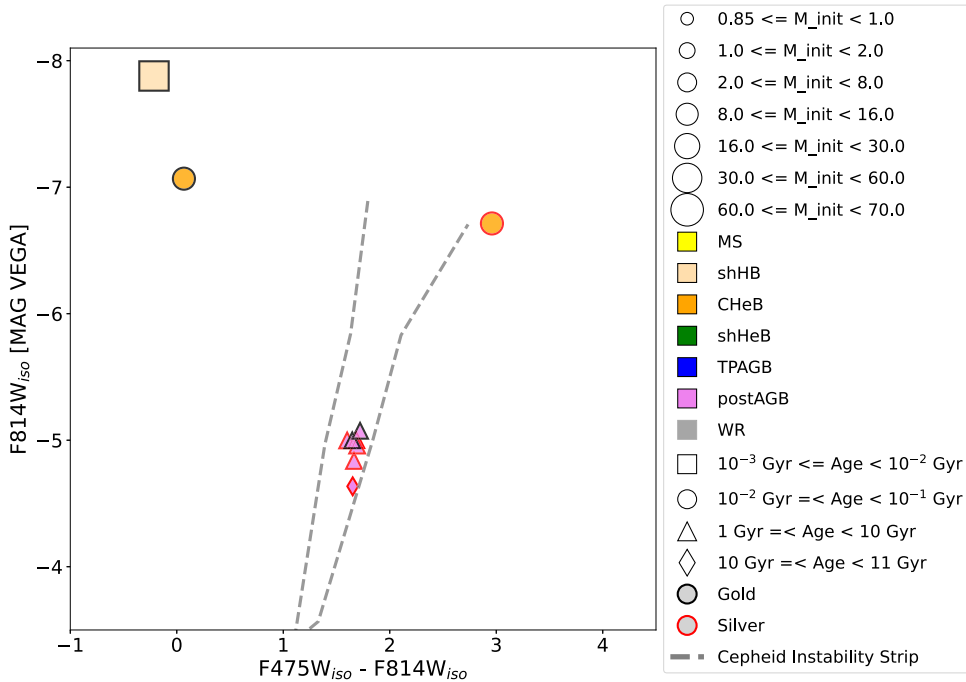


Figure 15. F475W – F814W color–absolute magnitude diagram of the four *Gold* (black-edged points) and eight *Silver* (red-edged points) confirmed M31 cluster-variable stars, using the theoretical color and magnitude values from the most likely point on their host cluster isochrone. Stellar evolutionary phase, initial mass, and host cluster age are denoted by marker color, marker size, and marker shape, respectively. The theoretical Cepheid instability strip is obtained from G. Fiorentino et al. (2002).

The remaining five TPAGB stars in our sample all have significantly fainter magnitudes ($F814W \gtrsim -5.5$ mag) and low initial masses in the range $1.0\text{--}1.3 M_{\odot}$. All five of these fainter TPAGBs are *Bronze* class, with four being *highly likely blended* and one being *likely blended*. The late evolutionary phase and low initial mass of these stars appear consistent with the properties of Mira variables (e.g., M. J. Ireland et al. 2004)—though only one star has an $F814W$ light-curve amplitude close to that of the 2.5 mag optical magnitude threshold indicative of Mira variability at 1.9 mag (J. A. Mattei 1997; L. A. Willson 2012; P. Iwanek et al. 2021), the PHAT amplitudes of the other four stars ranging between 0.29 and 0.72 mag. The single TPAGB with Mira-like $F814W$ amplitude is among the *highly likely blended* grouping, meaning that blending effects may contribute to this increased amplitude. However, the sparseness of the light-curve data available in this study only provides a lower limit on the light-curve amplitudes for the stars in our sample, particularly compared to the potential \sim 150–1000 day periods of Miras. The characteristic Mira variability of >2.5 mag in optical wavelengths should make verification of these TPAGB stars as Mira variables relatively straightforward using observations designed to account for the longer variability periods of Miras (P. Iwanek et al. 2021).

We find that the three CHeB stars residing within the same host cluster return identical theoretical isochrone color–magnitude properties of $F475W - F814W \sim 2$ and $F814W \sim -3.8$, as shown in Figure 16. Based on their colors, fainter magnitudes, and core helium-burning evolutionary phase, these stars appear consistent with BL Herculis variable stars. BL Herculis variables are the least luminous members of the Type II Cepheids, moving blue-to-red along the asymptotic giant branch with a helium-burning core, unlike the higher-luminosity later-stage W Virginis Type II Cepheids, which undergo shell helium

burning (A. Bhardwaj 2020). BL Herculis variables pulsate with the shortest observed periods of Type II Cepheids at \lesssim 5 days (G. Wallerstein 2002; I. Soszyński et al. 2008). However, the $\sim 1 M_{\odot}$ initial mass of the three CHeB stars in our sample is higher than the $\sim 0.5\text{--}0.6 M_{\odot}$ typically assumed for BL Herculis variables (e.g., M. Marconi & M. Di Criscienzo 2007), though more recent models have shown that masses $\gtrsim 0.7 M_{\odot}$ are required to facilitate observed first-overtone-only pulsation (I. Soszyński et al. 2019). Our analysis also shows the photometry of all three CHeB stars to be *highly likely blended* or *likely blended*, potentially contributing to their measured PHAT photometry being \sim 2 mag brighter than their isochrone-derived values and, in turn, producing their larger ellipse scaling factors (one $11\times$ and two $14\times$). We therefore tentatively designate these three CHeB stars as BL Herculis variables based on the available PHAT photometry, with additional observations required to verify their photometry and examine their potential period–luminosity relation for Type II Cepheid characteristics.

We classify the single, *Bronze* shHB star with $F475W - F814W \sim 1.6$, $F814W \sim -5.8$, and initial mass $9.8 M_{\odot}$ as a yellow supergiant. Its close proximity to the theoretical Cepheid instability strip calculated by G. Fiorentino et al. (2002), as shown in Figures 15 and 16, and the transition to helium-burning processes inherent to this variable star class make it consistent with a classical Cepheid variable. We note that there is no one-to-one correspondence between the inferred masses of our variable stars and the masses of the models used to construct the instability strip boundaries in G. Fiorentino et al. (2002). We primarily use these models for an approximate demarcation of the yellow belt on the CMD where unstable pulsation modes are excited.

The remaining cluster-variable stars in our sample all exhibit bluer isochrone-derived colors ($F475W - F814W \lesssim 1.4$). We

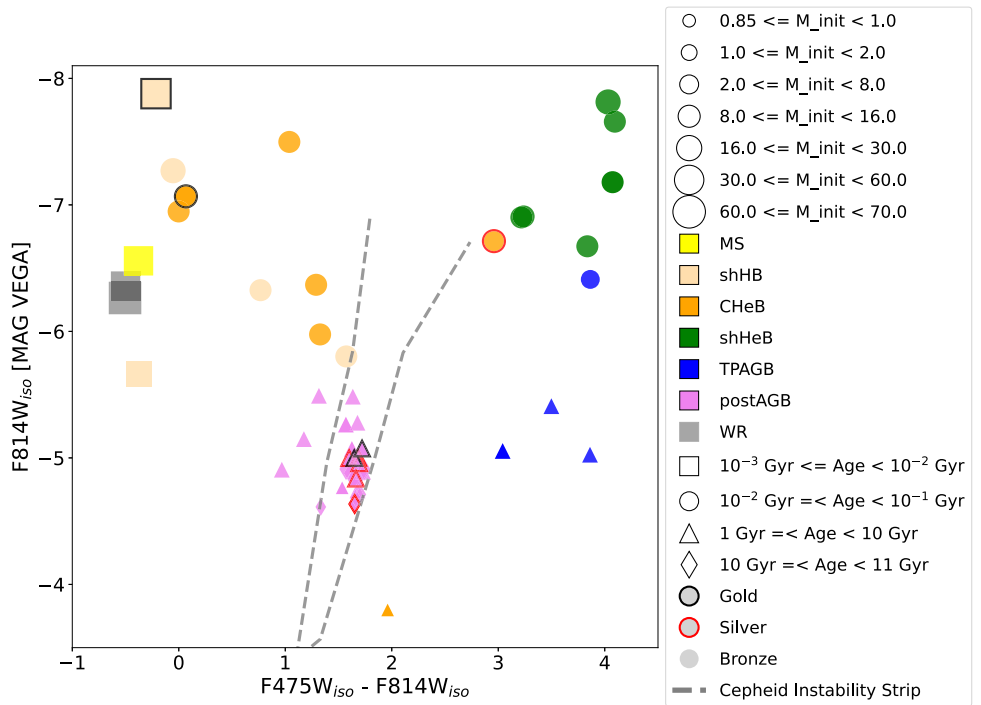


Figure 16. F475W – F814W color–absolute magnitude diagram of all 86 confirmed M31 cluster-variable stars, using the theoretical color and magnitude values from the most likely point on their host cluster isochrone. Stellar evolutionary phase, initial mass, and host cluster age are denoted by marker color, marker size, and marker shape, respectively. Marker edge colors denote their overall categorization into *Gold* (black-edged points), *Silver* (red-edged points), and *Bronze* (no edge color), as described in Section 4.3. The theoretical Cepheid instability strip is obtained from G. Fiorentino et al. (2002).

designate the single *Bronze*-class, *likely blended* MS variable star in this region of the CMD (see Figure 16) with initial mass $\sim 33 M_{\odot}$ as a β Cephei variable. These variable stars undergo *p*-mode pulsations driven by the κ -mechanism at the iron opacity bump (e.g., P. Moskalik & W. A. Dziembowski 1992; A. Miglio et al. 2007; H. Saio et al. 2013). The F475W and F814W light curves for this MS variable star are shown in Figure 17. The four shHB stars with $F475W - F814W < 1$ and initial stellar masses $11 M_{\odot} < M_{\text{init}} < 34 M_{\odot}$ comprise three *Bronze*-class results and one *Gold*-class result. We classify these four shHB stars as slowly pulsating B-type “supergiants” (SPBsgs)—*g*-mode-pulsating variable stars distinct from α Cygni variables (H. Saio et al. 2006; J. Daszynska-Daszkiewicz et al. 2013). These authors examined stellar evolutionary models for $7-20 M_{\odot}$ stars, finding that *g*-mode excitation is possible in post-MS stars at a broad range of effective temperatures for masses $\gtrsim 9 M_{\odot}$. It is possible that *p*-modes are excited simultaneously in some of these shHB stars, as there is some overlap in the instability regions of the SPBsg and β Cephei classes (see, e.g., H. Saio et al. 2006)—those stars will therefore be hybrids of the two classes. An example light curve for one of the shHB stars in our sample is shown in Figure 17.

The six blue CHeB stars comprise one *Gold* and five *Bronze* results, with the *Gold*-class star having the same color ($F475W - F814W = 0$) and magnitude ($F814W = -7$) values as a *Bronze* CHeB star. These six CHeB stars are divided into two fainter stars, with $F814W > -6.5$ and colors $1 < F475W - F814W < 1.5$, and four more-luminous stars, with $F814W < -6.5$ and a broader $0 < F475W - F814W < 1$ color range. The $\sim 8-16 M_{\odot}$ initial mass range of these six CHeB stars indicates that they may also be SPBsg stars, though in the core helium-burning phase rather than hydrogen shell-

burning (see J. Ostrowski & J. Daszynska-Daszkiewicz 2015). We note, however, that the median F814W amplitude of 0.21 mag for the combined set of blue shHB and CHeB variable stars in our sample is larger than that for the single SPBsg known so far (HD 163899; see H. Saio et al. 2006). Processes such as mass loss, rotational mixing, core contraction, etc. can also lead to a blueward evolution of massive stars after the RSG phase before core-helium exhaustion (H. Saio et al. 2013; G. Meynet et al. 2015). In particular, H. Saio et al. (2013) found that many pulsation modes can be excited in these post-RSGs in the blue region, with such stars constituting the α Cygni variable class. The two fainter ($F814W > -6.5$ mag), *Bronze*-class CHeB stars have initial masses in the range $\sim 8-10 M_{\odot}$. Modeling has shown that stars in this mass range can undergo extensive blue loops; see, for example, Figure 4 of S. Ekström et al. (2012). Examining the MIST-generated stellar evolutionary tracks of these fainter CHeB stars shows that the most probable isochrone points for both stars reside on their respective blue loops. We therefore classify the four more-luminous, blue CHeB stars as SPBsgs, while the two fainter, blue CHeBs are likely α Cygni variables—though it is unclear if their luminosity-to-mass ratio is large enough to excite pulsations (see H. Saio et al. 2013). Detailed frequency analysis via follow-up observations of these fainter stars would help to robustly identify their pulsation modes and verify their variable class type.

Finally, the two *Bronze* W-R stars in our sample have the largest initial stellar masses in our sample at $\sim 52 M_{\odot}$ and $\sim 66 M_{\odot}$. W-R stars have high mass-loss rates due to their strong stellar winds (C. H. Poe et al. 1989), with variability observed over ranges of hours to days (e.g., J. A. Toalá et al. 2022). The variability of W-R stars in M31 has previously been studied by M. D. Soraisam et al. (2020), with the variability of

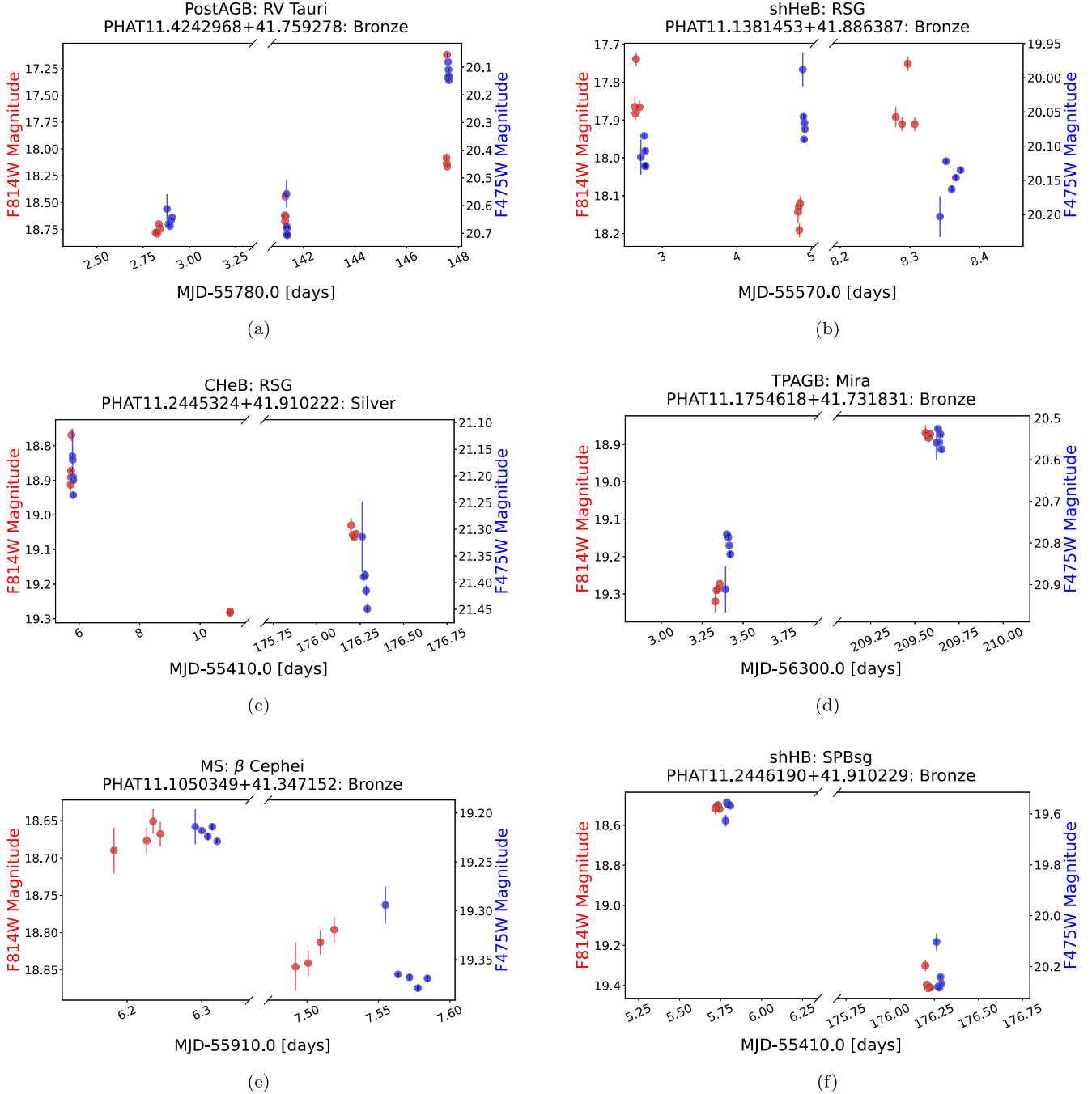


Figure 17. Light curves representing our variable stars in different evolutionary phases and variability classes including (a) RV Tauri, (b) RSG, (c) classical Cepheid, (d) Mira, (e) β Cephei, and (f) SPBsg.

W-R stars attributed to a combination of line-driven instabilities producing inhomogeneities in their stellar wind, rotation-driven perturbations in their winds, and pulsation instabilities (C. H. Poe et al. 1989; N. St-Louis et al. 2009; J. A. Toalá et al. 2022).

4.5. Caveats

There are a number of important caveats to highlight when considering the results produced from this work. We summarize these key points below.

1. It is important to emphasize that the photometry of all cluster stars in the PHAT survey will still be affected by

blending to some extent, including all the cluster-variable stars in our sample, regardless of blending probability. Ideally, the use of sophisticated deblending software may allow for the flux from a single source to be obtained; however, the variation in crowding across cluster environments would necessitate careful treatment of each detected source to accurately deblend the measured photometry. This is beyond the scope of the present study. Nevertheless, it is notable that we were still able to detect variable sources within these crowded cluster environments through our difference image analysis, despite the prevalence of blending in the measured PHAT photometry.

2. As noted previously—and demonstrated by Figures 8, 9, and 17—the sparseness of the PHAT survey photometry means that only lower limits on stellar light-curve amplitudes can be produced from PHAT survey data, impacting this study in two key ways. First, some cluster-variable stars detectable by the PHAT survey are likely not to have been identified, either due to being at the minimum phase in their light curve when observed or due to an insufficiently long baseline of observations being taken, precluding their detection. Second, the lower limits on light-curve amplitudes mean that the equilibrium point in color–magnitude space for a given cluster-variable star will be subject to greater uncertainty. This will also affect identification of the most probable isochrone datum for the star and therefore its initial mass and evolutionary phase (Section 4.2). Obtaining accurate light curves for the stars in the PHAT survey, for example through a long-baseline extension of the PHAT survey, would allow for these uncertainties to be reduced as well as provide huge potential for further variable star identification and subsequent classification.
3. The results presented in this work are also highly dependent upon the accuracy of literature cluster properties and the published isochrone models used. Inaccuracies in either of these dependencies will naturally impact the results obtained. The most notable effects would originate from the use of incorrect cluster properties based on solar versus nonsolar metallicity estimates and the inability of isochrone models to accurately account for the various mechanisms driving stellar variability. An attempt at the latter could be explored by building stellar variability into models of host cluster isochrones based on empirical measurements, such as from this work, and these modified isochrones then being used to examine the expected variable behavior over a given timescale. Even with the dependencies described above, however, and despite the limitations inherent to the sparse sampling of the PHAT survey data, the variable stars identified in this study show remarkable alignment with the initial masses and evolutionary phases of known variable stars.
4. Similarly, and as noted in our investigation into the effects of uncertainty on host cluster properties, there is a general lack of formally derived uncertainty estimates for host cluster age, metallicity, and extinction in the literature. Our analysis using the consistency between independent studies to derive uncertainty estimates in Section 4.2 provides an indication of the effects of varying these parameters for a representative host cluster—however, the limited number of host clusters common to both studies precludes more thorough analysis across all clusters in our sample. Our conclusions on the overall effects of varying cluster properties on the isochrone-derived variable star parameters are therefore limited without formal uncertainties for each host cluster.
5. We also assume that all cluster-variable stars in our sample are single-star systems when generating isochrones and evolutionary tracks. The evolution of binary or multistar systems is expected to follow the same path as their single-star counterparts, provided their stellar orbits are sufficiently separated and therefore noninteracting. When interactions occur—for example, mass transfer or tidal interactions—the evolutionary path of

both stars involved can be significantly altered compared to single-star systems depending on their initial stellar and orbital properties, with such interactions contributing to the more exotic known star types (see, for example, J. R. Hurley et al. 2002, and references therein). The global binary fraction ranges from 10% to 50% in globular clusters (A. Sollima et al. 2007) and 35% to 70% in open clusters (A. Sollima et al. 2010). The binary fraction for massive stars is 1.0 ± 0.2 , with 80%–90% likely to interact with a companion, while for lower-mass, e.g., solar-type, stars, the binary fraction is ~ 0.08 , with $15\% \pm 3\%$ likely to experience binary interactions (M. Moe & R. Di Stefano 2017). Hence, our massive-star results are likely to be sensitive to the models used, but we do not expect our low-mass star results to be dramatically affected by using single-star models. That said, the crowded nature of the cluster environments makes even verifying the multiplicity of star systems identified within our sample a challenge.

6. In using a single set of derived literature age and metallicity values for each cluster in this study, we are also making the assumption that the cluster and its constituent stars are coevolved. Observations of clusters show increasing evidence of multiple populations of distinct age and metallicity being produced within cluster environments (see, for example, A. P. Milone & A. F. Marino 2022). Investigating this possibility and its potential effects on our results is beyond the scope of this work; however, an extension of this study could be conducted should multiple populations be identified in the host clusters analyzed in this work.

5. Future Direction of Work

We have specifically focused on variable stars in M31 stellar clusters in this work, generating isochrones using estimates of host cluster age, extinction, and metallicity from which we have inferred the evolutionary phases and initial masses for the variable stars in our sample. Our next study will identify field variable stars in the M31 PHAT footprint using the knowledge gained from applying the DI pipeline in this work. Before proceeding with this next study, we first identify potential areas for improvement in our methodology by comparing our DI pipeline difference images to those produced by a cross-filtering convolution method (A. Gal-Yam et al. 2008) using the photutils “effective PSF” (ePSF) generation routine (J. Anderson & I. R. King 2000). These methods were chosen due to ePSFs having supplanted the TinyTim (J. Krist 1993) Hubble PSF-generating software for ACS observations,¹⁵ while cross-filtering convolution allows for comparisons with DI pipeline results without extensively altering the OIS method to use ePSFs.

We select six science-template image pairs and their pipeline difference images for investigation. Each set of images is associated with a different cluster and selected to create a representative sample of potential DI pipeline behavior, with two “good” (minimal artifacts), two “poor” (extended, brighter residuals), and two misaligned subtractions. Reference sources required for ePSF generation are obtained from background-subtracted science and template frames, obtained by

¹⁵ <https://www.stsci.edu/hst/instrumentation/focus-and-pointing/focus/tiny-tim-hst-psf-modeling>

reprojecting and aligning each pair of science and template frames in the same way described for the DI pipeline in Section 3.4.1, before estimating the background of each frame. PSF reference sources are then detected in each background-subtracted frame using `find_peaks` from `photutils` with a threshold value of 2. We visually assess cutouts of each potential reference source for crowding, contamination, and stellar-like behavior, excluding those sources contaminated within a 5 pixel radius of the peak. Isolated, stellar-like sources are used in `photutils ePSFBuilder` to generate accurate ePSF models for the frame. We vary the `ePSFBuilder` sigma clipping, maximum iteration, and input cutout size (but no oversampling) to identify the best parameter values for accurate ePSF model generation, obtaining the best results using 9 pixel diameter cutouts, 3σ clipping, and 50 max. iterations. We then convolve the science frame with the template ePSF, and vice versa, background matching the convolved frames by subtracting the convolved template frame from the convolved science frame and using this intermediate difference image to produce a `Background2D` map that is added to the convolved template frame. The difference image process is then repeated and the result compared to the DI pipeline difference image through visual inspection and image statistics measured within a 75×75 pixel region centered on the host cluster in each difference image.

Figure 18 shows example DI pipeline versus convolved ePSF difference images for science-template frame pairs. We find that the ePSF difference images show a general improvement in image statistics, with the strength of over- and undersubtraction substantially improved. That said, the ePSF results are strongly dependent on input PSF behavior, particularly for very crowded clusters, e.g., cluster 212 in Figure 18. Small deviations from stellar behavior in input PSFs can produce inaccuracies in the ePSF model, leaving residual patterns around sources in the difference images. Even with this dependence on input PSF behavior, the improvements shown by the ePSF results look promising. We will consider adopting and further refining the ePSF-based convolution method in upcoming studies searching for M31 variable field stars; this will require automation of input PSF selection due to the larger data set to be analyzed. We will also investigate the “proper image subtraction” (“ZOGY”) method developed by B. Zackay et al. (2016), including its built-in PSF extraction, as an alternative to the ePSF convolution method.

Aside from applying our results to future studies, our results highlight the enormous potential of well-sampled, long-base-line observations. Though sparsely sampled, our analysis of M31 stellar clusters in the PHAT survey has nevertheless produced valuable results and potential targets for follow-up observations. A purpose-built time-domain survey of a similar scope to the PHAT survey with a space mission would allow for many of the variable stars in this work to be verified, provide further constraints on the properties of longer-period variables, and likely result in additional candidate and confirmed variable stars. The upcoming Roman Observatory holds enormous potential for such a study, as highlighted by the proposed *RomAndromeda* survey (A. Dey et al. 2023). Though a similarly sparse sampling to the PHAT survey, the proposed *RomAndromeda* survey complements PHAT and allows for shorter-period variable stars to be identified at magnitudes fainter than the PHAT survey ($F146 < 25.3$, $F062 < 24.8$ AB mag; A. Dey et al. 2023) within the first

year of Roman operations. This could feasibly be expanded to identifying longer-period variables in M31 observations should the Roman mission be extended and additional observing epochs obtained.

6. Conclusions

We exploit the photometric depth and spatial resolution of HST to systematically identify variable stars within M31 stellar clusters using the PHAT survey data. Out of 294,981 stars in 2753 M31 clusters, we identify 239 luminous ($F814W < 19$ mag) candidate variable stars via statistical analysis of their sparse PHAT light curves. The highly crowded environments of the M31 stellar clusters present a challenge for visually vetting the candidates. We therefore utilize DI to verify PHAT light-curve variability and confirm 86 cluster-variable stars after removing three likely foreground stars through cross-matching with Gaia DR3. We use the MIST web interpolator to generate an isochrone for each host cluster based on properties available in the literature. We match each confirmed variable star to the most probable point on its host cluster isochrone, finding initial stellar masses in the range $0.8\text{--}67 M_{\odot}$ for the 86 stars in our sample. In terms of evolutionary phase, we find that the majority of the variable stars are in the post-AGB phase, while the remaining stars are distributed across the MS phase and more evolved hydrogen- and helium-burning phases.

For the first time, we use the initial mass and evolutionary phase inferred from host cluster isochrones to assign a variable class to each star in our sample. We attribute the stars in more evolved hydrogen- and helium-burning phases to a mixture of β Cephei variables, SPBsgs, and candidate α Cygni variables. We find eight RSG variable stars in our sample, five of which have been previously identified by L. C. Johnson et al. (2012), which we confirm through their variability, alongside a candidate SAGB star based on its RSG-like luminosity, red color, and $\sim 8 M_{\odot}$ initial mass. We also identify numerous RV Tauri variables, along with smaller numbers of candidate Mira variables, a likely classical Cepheid, BL Herculis variables, and W-R stars. We calculate the probability of measured PHAT photometry being blended for each of our cluster-variable stars, which we consider along with the quality of the difference image source detections to inform our level of confidence in their attributed properties. From this analysis, we characterize the properties of 12 cluster-variable stars in our sample—nine RV Tauri stars, two SPBsg stars, and one RSG—with higher confidence.

We caution that this work is dependent upon the accuracy of the published isochrone models and cluster properties used, in addition to PHAT survey photometry of all cluster stars remaining subject to blending effects and uncertainties in derived stellar properties due to the sparse PHAT light-curve data. That said, our results show a remarkable consistency with known variable classes, indicating the potential for discoveries from a purpose-built, well-sampled PHAT-like time-domain survey with an extended time baseline. The Roman Observatory holds enormous potential for studying variable stars in M31, with the proposed *RomAndromeda* survey (A. Dey et al. 2023) allowing for short-period variables at fainter magnitudes than those in the PHAT survey to be identified within 1 yr of Roman operations commencing, with potential expansion to longer-period variables should the mission be extended.

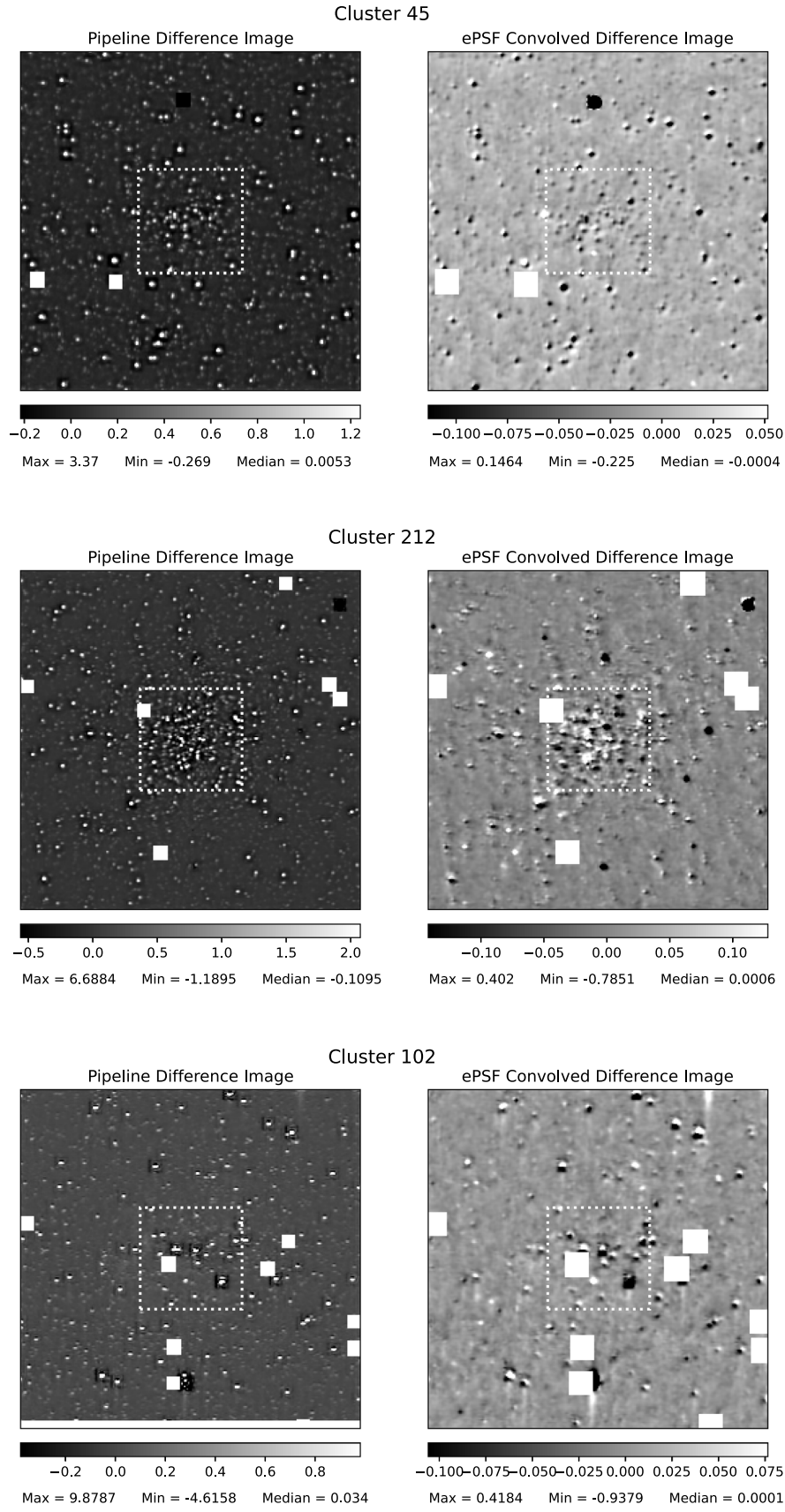


Figure 18. DI pipeline (left) and ePSF-based (right) difference images produced for three of the six test cases used to identify potential improvements using ePSF models. Areas surrounded by the white dashed line denote the region of interest encapsulating each cluster within which image statistics are calculated.

Acknowledgments

We thank the anonymous reviewer for the valuable feedback. Based on observations with the NASA/ESA Hubble Space Telescope obtained from the Mikulski Archive for Space Telescopes (MAST) at the Space Telescope Science Institute (STScI), which is operated by the Association of Universities for Research in Astronomy, Inc., under NASA contract NAS5-26555. Support for Program No. HST-AR-17064 was provided through a grant from the STScI under NASA contract NAS5-26555. P.T., S.Z., and J.L. conducted this research under the auspices of the Science Internship Program (SIP) at UCSC.

Software: Astro Data Lab (M. J. Fitzpatrick et al. 2014), ARTES (T. Stolk et al. 2017), PICASO (N. E. Batalha et al. 2019), pandas (W. McKinney 2010), NumPy (S. van der Walt et al. 2011), IPython (F. Pérez & B. E. Granger 2007), Jupyter (T. Kluyver et al. 2016), matplotlib (J. D. Hunter 2007), astroalign (M. Beroiz et al. 2020a), astropy (Astropy Collaboration et al. 2018), optimal image subtraction (OIS; M. Beroiz et al. 2020b), scikit learn (F. Pedregosa et al. 2011)

Appendix A Astro Data Lab Access

The NSF NOIRLab Astro Data Lab (M. J. Fitzpatrick et al. 2014) is an online astronomical data storage and analysis service.¹⁶ A free Astro Data Lab user account is required to access the data used in this work¹⁷ which will then need to be verified by the Astro Data Lab Team before the service can be accessed.¹⁸

Appendix B Accessing Data from This Work

The data used in this work are stored in the public directory on Astro Data Lab’s JupyterLab service. A JupyterLab session is opened using the “Launch a Jupyter Notebook” button or under the Quick Start menu on the Astro Data Lab homepage. In JupyterLab, a Python 3 environment and kernel can be initiated from the Launcher window to access the data directory. The data used in this work are stored in the public directory `aspatel://public/data_products`, accessible through the Astro Data Lab client using the following Python 3 cell commands:

```
from dl import authClient as ac, storeClient as sc
auth_token = ac.login('YOUR_USERNAME','YOUR_PASSWORD')
sc.ls("aspatel://public/data_products")
```

using your Astro Data Lab username and password in place of `YOUR_USERNAME` and `YOUR_PASSWORD`, respectively.¹⁹ Running the above cell will return a list of directories and files: `README`, `lcs.dat`, `tab2.dat`, `tab3.dat`.

1. `tab2.dat` contains the catalog of 239 candidate cluster-variable stars identified through light-curve analysis described in Section 3.2.
2. `tab3.dat` contains the final sample of 86 confirmed cluster-variable stars along with their inferred evolutionary phases, initial masses, and host cluster properties.
3. `lcs.dat` contains the light-curve data for all 239 candidate cluster-variable stars identified through light-curve analysis described in Section 3.2.

All of the details regarding these tables are provided in the `README` file.

The data, tables, and `README.txt` files can be copied from `aspatel://public/data_products` into another directory under a different user with the command

```
sc.get("aspatel://public/data_products/" , "../DESTINATION_DIRECTORY")
```

using the name of your directory to store all data products in place of `../DESTINATION_DIRECTORY`.

Appendix C Accessing Additional PHAT Survey Data

Additional data from the `phot_meas` and `phot_mod` tables, which hold the *per-exposure* and *combined* (across exposures) photometric measurements from the PHAT survey, respectively, stored on Astro Data Lab can be accessed using the `QueryClient` in JupyterLab. The example code block below demonstrates how to retrieve all data from `phot_meas` (`query_all`) versus specific column values (`query_cols`) for a given PHAT target, returning the results of each query as `pandas` data frames. Our `phot_meas` queries include `magvega < 99.0` to filter exposures with nondetections and the sharpness threshold `sharp^2 < 0.2` to exclude

¹⁶ Accessible at <https://datalab.noirlab.edu/>.

¹⁷ This can be generated at <https://datalab.noirlab.edu/account/register.html>.

¹⁸ Further information on Astro Data Lab can be found at <https://datalab.noirlab.edu/docs/manual/index.html> and via the User Forum at <https://datalab.noirlab.edu/help/>.

¹⁹ Further information on using and accessing data from the Astro Data Lab StoreClient, including commands, is provided at <https://datalab.noirlab.edu/docs/manual/UsingAstroDataLab/ClientInterfaces/StoreClient/StoreClient.html>.

measurements affected by cosmic-ray strikes, bad pixels, etc. as described in Section 3.1.²⁰ The phot_mod table can be queried by changing the phot_meas entry in the code block, along with any relevant table column headers specified in the query.

```

phat_id = "PHAT_10.9517775+41.448073"

query_all = """SELECT *
    FROM phat_v2.phot_meas
    WHERE objid = '%s' AND filter = 'F814W' AND magvega < 99.0 and sharp ^2 < 0.2
    """%phat_id

try:
    result1 = qc.query(auth_token, sql = query_all, timeout = 400)
except Exception as e:
    print(e)
df_all = helpers.utils.convert(result1,'pandas')

query_cols = """SELECT mjd, magvega, magerr,sharp
    FROM phat_v2.phot_meas
    WHERE objid = '%s' AND filter = 'F814W' AND magvega < 99.0 and sharp ^2 < 0.2
    """%phat_id

try:
    result2 = qc.query(auth_token, sql = query_cols, timeout = 400)
except Exception as e:
    print(e)
df_cols = helpers.utils.convert(result2,'pandas')

```

Appendix D Foreground Star Identification

We cross-match our initial sample of 376 luminous ($F814W < 19$ mag) PHAT cluster stars (see Table 1) with the Gaia DR3 catalog available through Astro Data Lab²¹ using a search radius of $0.^{\circ}11$, comparable to the FWHM of the PSF for both ACS (M. Santiago-Cortés et al. 2010) and Gaia (C. Fabricius et al. 2016). We obtain 204 PHAT stars with Gaia counterparts.

We designate potential foreground stars in the resulting sample using the same criteria described by P. Barmby (2023), with foreground stars having either (i) significant nonzero parallax and proper motion inconsistent with that of M31, or (ii) significant nonzero proper motion also inconsistent with that of M31. We adopt a significance level of $n = 10$ below. We determine the significant nonzero parallax condition by adopting the zero-point-corrected parallax signal-to-noise ratio described in P. Barmby (2023):

$$\left| \frac{\bar{\omega} + 0.017}{\sigma_{\bar{\omega}}} \right| > n, \quad (\text{D1})$$

where $\bar{\omega}$ and $\sigma_{\bar{\omega}}$ are the parallax and parallax error in mas, respectively, and 0.017 mas is the median parallax zero-point of Gaia DR3 determined by L. Lindegren et al. (2021). The significant nonzero proper motion condition is determined following

$$[\mu_{\text{R.A.}}, \mu_{\text{decl.}}] \text{Cov}^{-1} \begin{bmatrix} \mu_{\text{R.A.}} \\ \mu_{\text{decl.}} \end{bmatrix} > n^2, \quad (\text{D2})$$

which can be queried directly from the Gaia DR3 databases, as detailed in P. Barmby (2023), where $\mu_{\text{R.A.}}$ and $\mu_{\text{decl.}}$ are the R.A. and decl. proper motions of the star in mas yr^{-1} , respectively. We use the proper motion of M31 measured by J. B. Salomon et al. (2021; 48.9 ± 10.5 mas and -36.9 ± 8.1 mas in R.A. and decl., respectively) to check for inconsistency between the stellar proper motions with that of M31.

Of the 204 luminous cluster stars in the PHAT catalog with cross-matched counterparts in Gaia DR3, 142 stars have parallax and proper motion measurements in Gaia DR3, of which seven stars meet the foreground star criteria defined above. Our analysis of these stars described in Section 3.4.3 reveals that three of the foreground stars—PHAT_11.1765404+41.919860, PHAT_11.3058193+41.626605 and PHAT_11.0161713+41.276141—have difference image source detections. We thus exclude these three stars from our 89 confirmed cluster-variable stars identified in Section 3.4.3. Of the remaining 86 cluster-variable stars, we note that 47 of them are included in the above sample of 204 stars with Gaia DR3 counterparts, one of which—PHAT_10.9665814+41.263916—has also been observed to be variable with Gaia.

²⁰ The columns available for query are described at https://datalab.noirlab.edu/query.php?name=phat_v2.phot_mod for phot_mod and https://datalab.noirlab.edu/query.php?name=phat_v2.phot_meas for phot_meas.

²¹ <https://datalab.noirlab.edu/gaia.php>

ORCID iDs

- Richard Smith [ID](https://orcid.org/0000-0002-3346-2370) <https://orcid.org/0000-0002-3346-2370>
 Avi Patel [ID](https://orcid.org/0009-0000-5120-1193) <https://orcid.org/0009-0000-5120-1193>
 Monika D. Soraisam [ID](https://orcid.org/0000-0001-6360-992X) <https://orcid.org/0000-0001-6360-992X>
 Puragra Guhathakurta [ID](https://orcid.org/0000-0001-8867-4234) <https://orcid.org/0000-0001-8867-4234>
 Pranav Tadepalli [ID](https://orcid.org/0009-0008-2161-0509) <https://orcid.org/0009-0008-2161-0509>
 Sally Zhu [ID](https://orcid.org/0000-0002-2624-1107) <https://orcid.org/0000-0002-2624-1107>
 Joseph Liu [ID](https://orcid.org/0009-0007-8904-4139) <https://orcid.org/0009-0007-8904-4139>
 Léo Girardi [ID](https://orcid.org/0000-0002-6301-3269) <https://orcid.org/0000-0002-6301-3269>
 L. Clifton Johnson [ID](https://orcid.org/0000-0001-6421-0953) <https://orcid.org/0000-0001-6421-0953>
 Sagnick Mukherjee [ID](https://orcid.org/0000-0003-1622-1302) <https://orcid.org/0000-0003-1622-1302>
 Knut A. G. Olsen [ID](https://orcid.org/0000-0002-7134-8296) <https://orcid.org/0000-0002-7134-8296>
 Benjamin F. Williams [ID](https://orcid.org/0000-0002-7502-0597) <https://orcid.org/0000-0002-7502-0597>

References

- Alcock, C., Allsman, R. A., Alves, D. R., et al. 1998, *AJ*, **115**, 1921
 Anderson, J., & King, I. R. 2000, *PASP*, **112**, 1360
 Anderson, R. I., Saio, H., Ekström, S., Georgy, C., & Meynet, G. 2016, *A&A*, **591**, A8
 Astropy Collaboration, Price-Whelan, A. M., Sipőcz, B. M., et al. 2018, *AJ*, **156**, 123
 Barnby, P. 2023, *MNRAS*, **518**, 3746
 Batalha, N. E., Marley, M. S., Lewis, N. K., & Fortney, J. J. 2019, *ApJ*, **878**, 70
 Bernard, E. J., Ferguson, A. M. N., Barker, M. K., et al. 2012, *MNRAS*, **420**, 2625
 Beroiz, M., Cabral, J., & Sanchez, B. 2020a, *A&C*, **32**, 100384
 Beroiz, M., Sánchez, B., & Iyer, V. 2020b, toros-astro/ois: v0.2, Zenodo, doi:[10.5281/zenodo.4042147](https://doi.org/10.5281/zenodo.4042147)
 Bhardwaj, A. 2020, *JApA*, **41**, 23
 Bódi, A., & Kiss, L. L. 2019, *ApJ*, **872**, 60
 Bono, G., Marconi, M., Cassisi, S., et al. 2005, *ApJ*, **621**, 966
 Bradley, L., Sipőcz, B., Robitaille, T., et al. 2023, astropy/photutils: v1.8.0, Zenodo, doi:[10.5281/zenodo.7946442](https://doi.org/10.5281/zenodo.7946442)
 Buchler, J. R., & Kovacs, G. 1987, *ApJL*, **320**, L57
 Caldwell, N., Schiavon, R., Morrison, H., Rose, J. A., & Harding, P. 2011, *AJ*, **141**, 61
 Choi, J., Dotter, A., Conroy, C., et al. 2016, *ApJ*, **823**, 102
 Conroy, C., Strader, J., van Dokkum, P., et al. 2018, *ApJ*, **864**, 111
 Cordiner, M. A., Cox, N. L. J., Evans, C. J., et al. 2011, *ApJ*, **726**, 39
 da Silva, L., Girardi, L., Pasquini, L., et al. 2006, *A&A*, **458**, 609
 Dalcanton, J. J., Williams, B. F., Lang, D., et al. 2012, *ApJS*, **200**, 18
 Daszynska-Daszkiewicz, J., Ostrowski, J., & Pamiatnykh, A. A. 2013, *MNRAS*, **432**, 3153
 de Meulenaer, P., Narbutis, D., Mineikis, T., & Vansevičius, V. 2015, *A&A*, **574**, A66
 de Meulenaer, P., Stonkutė, R., & Vansevičius, V. 2017, *A&A*, **602**, A112
 Dey, A., Najita, J., Filion, C., et al. 2023, arXiv: [2306.12302](https://arxiv.org/abs/2306.12302)
 Doherty, C. L., Gil-Pons, P., Siess, L., & Lattanzio, J. C. 2017, *PASA*, **34**, e056
 Dolphin, A. E. 2000, *PASP*, **112**, 1383
 Dotter, A. 2016, *ApJS*, **222**, 8
 Ekström, S., Georgy, C., Eggenberger, P., et al. 2012, *A&A*, **537**, A146
 Fabricius, C., Bastian, U., Portell, J., et al. 2016, *A&A*, **595**, A3
 Feast, M. 1999, *PASP*, **111**, 775
 Ferguson, A. M. N., Johnson, R. A., Faria, D. C., et al. 2005, *ApJ*, **622**, L109
 Fiorentino, G., Caputo, F., Marconi, M., & Musella, I. 2002, *ApJ*, **576**, 402
 Fitzpatrick, M. J., Olsen, K., Economou, F., et al. 2014, *Proc. SPIE*, **9149**, 91491T
 Gal-Yam, A., Maoz, D., Guhathakurta, P., & Filippenko, A. V. 2008, *ApJ*, **680**, 550
 Galleti, S., Federici, L., Bellazzini, M., Fusi Pecci, F., & Macrina, S. 2004, *A&A*, **416**, 917
 González-Fernández, C., Asensio Ramos, A., Garzón, F., Cabrera-Lavers, A., & Hammersley, P. L. 2014, *ApJ*, **782**, 86
 Groenewegen, M. A. T., & Jurkovic, M. I. 2017, *A&A*, **604**, A29
 Heger, A., Jeannin, L., Langer, N., & Baraffe, I. 1997, *A&A*, **327**, 224
 Hekker, S., Basu, S., Stello, D., et al. 2011, *A&A*, **530**, A100
 Hirayama, D., Howell, D. A., Van Dyk, S. D., et al. 2021, *NatAs*, **5**, 903
 Hirschi, R., Meynet, G., & Maeder, A. 2004, *A&A*, **425**, 649
 Humphreys, R. M., Helmel, G., Jones, T. J., & Gordon, M. S. 2020, *AJ*, **160**, 145
 Hunter, J. D. 2007, *CSE*, **9**, 90
 Hurley, J. R., Tout, C. A., & Pols, O. R. 2002, *MNRAS*, **329**, 897
 Ireland, M. J., Scholz, M., Tuthill, P. G., & Wood, P. R. 2004, *MNRAS*, **355**, 444
 Iwanek, P., Kozłowski, S., Gromadzki, M., et al. 2021, *ApJS*, **257**, 23
 Johnson, L. C., Seth, A. C., Dalcanton, J. J., et al. 2012, *ApJ*, **752**, 95
 Johnson, L. C., Seth, A. C., Dalcanton, J. J., et al. 2015, *ApJ*, **802**, 127
 Johnson, L. C., Seth, A. C., Dalcanton, J. J., et al. 2017, *ApJ*, **839**, 78
 Jura, M. 1986, *ApJ*, **309**, 732
 Jurkovic, M. I. 2021, in ASP Conf. Ser. 529, RR Lyrae and Cepheid Conference 2019: Frontiers of Classical Pulsators, ed. K. Kinemuchi et al. (San Francisco, CA: ASP), **305**
 Kamath, D., Wood, P. R., Van Winckel, H., & Nie, J. D. 2016, *A&A*, **586**, L5
 Kang, Y., Rey, S.-C., Bianchi, L., et al. 2012, *ApJS*, **199**, 37
 Kiss, L. L., Derekas, A., Szabo, G., Bedding, T. R., & Szabados, L. 2007, *MNRAS*, **375**, 1338
 Kluyver, T., Ragan-Kelley, B., Pérez, F., et al. 2016, Positioning and Power in Academic Publishing: Players, Agents and Agendas (Amsterdam: IOS Press), **87**
 Kodric, M., Riffeser, A., Hopp, U., et al. 2013, *AJ*, **145**, 106
 Krist, J. 1993, in ASP Conf. Ser. 52, Astronomical Data Analysis Software and Systems II, ed. R. J. Hanisch, R. J. V. Brissenden, & J. Barnes (San Francisco, CA: ASP), **356**
 Krist, J. 2003, Instrument Science Report *ACS 2003-06*, STScI
 Lee, C. H., Riffeser, A., Koppenhoefer, J., et al. 2012, *ApJ*, **143**, 89
 Lim, S., Hwang, N., & Lee, M. G. 2013, *ApJ*, **766**, 20
 Lindegren, L., Klioner, S. A., Hernández, J., et al. 2021, *A&A*, **649**, A2
 Manick, R., Van Winckel, H., Kamath, D., Sekaran, S., & Kolenberg, K. 2018, *A&A*, **618**, A21
 Marconi, M., & Di Criscienzo, M. 2007, *A&A*, **467**, 223
 Marshall, D. J., Robin, A. C., Reylé, C., Schultheis, M., & Picaud, S. 2006, *A&A*, **453**, 635
 Massey, P., Armandroff, T. E., & Conti, P. S. 1986, *AJ*, **92**, 1303
 Mattei, J. A. 1997, *JAAVSO*, **25**, 57
 McConnachie, A. W., Irwin, M. J., Ferguson, A. M. N., et al. 2005, *MNRAS*, **356**, 979
 McConnachie, A. W., Irwin, M. J., Ibata, R. A., et al. 2009, *Natur*, **461**, 66
 McKinney, W. 2010, in 9th Python in Science Conf., Data Structures for Statistical Computing in Python, ed. S. van der Walt & J. Millman, **56**
 Meynet, G., Chomienné, V., Ekström, S., et al. 2015, *A&A*, **575**, A60
 Meynet, G., & Maeder, A. 2000, *A&A*, **361**, 101
 Medina, G. E., Lemasse, B., & Grebel, E. K. 2021, *MNRAS*, **505**, 1342
 Miglio, A., Brogaard, K., Stello, D., et al. 2012, *MNRAS*, **419**, 2077
 Miglio, A., Montalbán, J., & Dupret, M. A. 2007, *CoAst*, **151**, 48
 Miller, J. P., Pennypacker, C. R., & White, G. L. 2008, *PASP*, **120**, 449
 Milone, A. P., & Marino, A. F. 2022, *Univ*, **8**, 359
 Moe, M., & Di Stefano, R. 2017, *ApJS*, **230**, 15
 Moskalik, P., & Dziembowski, W. A. 1992, *A&A*, **256**, L5
 Mould, J., & Kristian, J. 1986, *ApJ*, **305**, 591
 Ngeow, C.-C., & Kanbur, S. M. 2004, *MNRAS*, **349**, 1130
 Olsen, K., Williams, B., Fitzpatrick, M., & PHAT Team 2018, AAS Meeting, **231**, 362.05
 Ostrowski, J., & Daszynska-Daszkiewicz, J. 2015, *MNRAS*, **447**, 2378
 Palakkatharappil, D. B., & Creevey, O. L. 2023, *A&A*, **674**, A146
 Peacock, M. B., Maccarone, T. J., Knigge, C., et al. 2010, *MNRAS*, **402**, 803
 Pedregosa, F., Varoquaux, G., Gramfort, A., et al. 2011, *JMLR*, **12**, 2825
 Percy, J. R. 2022, *JAAVSO*, **50**, 96
 Pérez, F., & Granger, B. E. 2007, *CSE*, **9**, 21
 Pinsonneault, M. H., Elsworth, Y. P., Tayar, J., et al. 2018, *ApJS*, **239**, 32
 Poe, C. H., Friend, D. B., & Cassinelli, J. P. 1989, *ApJ*, **337**, 888
 Pritchett, C. J., & van den Bergh, S. 1988, *ApJ*, **331**, 135
 Ryon, J. E. 2023, ACS Instrument Handbook for Cycle 31 v. 22.0 (Baltimore, MD: STScI)
 Saha, A., Vivas, A. K., Olszewski, E. W., et al. 2019, *ApJ*, **874**, 30
 Saio, H., Georgy, C., & Meynet, G. 2013, *MNRAS*, **433**, 1246
 Saio, H., Kuschnig, R., Gautschy, A., et al. 2006, *ApJ*, **650**, 1111
 Salomon, J. B., Ibata, R., Reylé, C., et al. 2021, *MNRAS*, **507**, 2592
 Salpeter, E. E. 1955, *ApJ*, **121**, 161
 Santiago-Cortés, M., Mayya, Y. D., & Rosa-González, D. 2010, *MNRAS*, **405**, 1293

- Senchyna, P., Johnson, L. C., Dalcanton, J. J., et al. 2015, *ApJ*, **813**, 31
- Sollima, A., Beccari, G., Ferraro, F. R., Fusi Pecci, F., & Sarajedini, A. 2007, *MNRAS*, **380**, 781
- Sollima, A., Carballo-Bello, J. A., Beccari, G., et al. 2010, *MNRAS*, **401**, 577
- Soraisam, M. D., Bildsten, L., Drout, M. R., et al. 2020, *ApJ*, **893**, 11
- Soraisam, M. D., Bildsten, L., Drout, M. R., et al. 2018, *ApJ*, **859**, 73
- Soszyński, I., Smolec, R., Udalski, A., & Pietrukowicz, P. 2019, *ApJ*, **873**, 43
- Soszyński, I., Udalski, A., Szymański, M. K., et al. 2008, *AcA*, **58**, 293
- St-Louis, N., Chené, A. N., Schnurr, O., & Nicol, M. H. 2009, *ApJ*, **698**, 1951
- Stolker, T., Min, M., Stam, D. M., et al. 2017, *A&A*, **607**, A42
- Takeuti, M., & Petersen, J. O. 1983, *A&A*, **117**, 352
- Templeton, M. R., McNamara, B. J., Guzik, J. A., et al. 1997, *AJ*, **114**, 1592
- Toalá, J. A., Bowman, D. M., Van Reeth, T., et al. 2022, *MNRAS*, **514**, 2269
- Turner, D., & Burke, J. 2007, *AJ*, **124**, 2931
- van der Walt, S., Colbert, S. C., & Varoquaux, G. 2011, *CSE*, **13**, 22
- Wagner-Kaiser, R., Sarajedini, A., Dalcanton, J. J., Williams, B. F., & Dolphin, A. 2015, *MNRAS*, **451**, 724
- Wallerstein, G. 2002, *PASP*, **114**, 689
- Wang, S., & Chen, X. 2019, *ApJ*, **877**, 116
- Wang, Y., Gao, J., & Ren, Y. 2022, *ApJS*, **259**, 12
- Williams, B. F., Dalcanton, J. J., et al. 2014, *ApJS*, **215**, 9
- Williams, B. F., Dolphin, A. E., Dalcanton, J. J., et al. 2017, *ApJ*, **846**, 145
- Williams, B. F., Olsen, K., Khan, R., Pirone, D., & Rosema, K. 2018, *ApJS*, **236**, 4
- Willson, L. A., & Marengo, M. 2012, *JAAVSO*, **40**, 516
- Zackay, B., Ofek, E. O., & Gal-Yam, A. 2016, *ApJ*, **830**, 27
- Zasowski, G., Majewski, S. R., Indebetouw, R., et al. 2009, *ApJ*, **707**, 510
- Zhang, R., Yuan, H., & Chen, B. 2023, *ApJS*, **269**, 6
- Zhuo, J., Deng, L.-C., Wang, K., et al. 2021, *RAA*, **21**, 227